HHS Public Access

Author manuscript

Nat Struct Mol Biol. Author manuscript; available in PMC 2021 May 09.

Published in final edited form as:

Nat Struct Mol Biol. 2021 January ; 28(1): 50–61. doi:10.1038/s41594-020-00522-0.

Mechanism of Auto-inhibition and Activation of Mec1^{ATR} Checkpoint Kinase

Elias A. Tannous[1,#], **Luke A. Yates**[2,#], **Xiaodong Zhang**[3,*], **Peter M. Burgers**[4,*]

[1]Department of Biochemistry and Molecular Biophysics, Washington University School of Medicine, Saint Louis, Missouri, USA

[2]Section of Structural Biology, Department of Infectious Diseases, Imperial College London SW7 2AZ, UK

[3]Section of Structural Biology, Department of Infectious Diseases, Imperial College London SW7 2AZ, UK

[4]Department of Biochemistry and Molecular Biophysics, Washington University School of Medicine, Saint Louis, Missouri, USA

Abstract

In response to DNA damage or replication fork stalling, the basal activity of *Saccharomyces cerevisiae* Mec1^{ATR} is stimulated in a cell cycle dependent manner, leading to cell cycle arrest and promoting DNA repair. Mec1^{ATR} dysfunction leads to cell death in yeast and causes chromosome instability and embryonic lethality in mammals. Thus, ATR is a major target for cancer therapies in homologous recombination-deficient cancers. Here we identify a single mutation in Mec1, conserved in ATR, that results in constitutive activity. Using cryo electron microscopy, we determined the structures of this constitutively active form (Mec1(F2244L)-Ddc2) at 2.8 Å, and the wild-type at 3.8 Å, both in complex with Mg^{2+}-AMP-PNP. These structures yield near complete atomic models for Mec1-Ddc2 and uncover the molecular basis for low basal activity and the conformational changes required for activation. Combined with biochemical and genetic data, we discover key regulatory regions and propose a Mec1 activation mechanism.

Keywords

Mec1/ATR; DNA damage response; checkpoint control; enzyme kinetics; serine/threonine protein kinase; cryoEM structures; activation mechanism

*co-corresponding authors.
#equal contribution.
Lead author: Peter M. Burgers: burgers@wustl.edu

Author Contributions

E.A.T., L.A.Y., X.Z., and P.M.B. planned this study. E.A.T. carried out the biochemical and genetic studies, and L.A.Y. carried out the structural studies. All authors were involved in the interpretation of the results and the writing of the paper, and approved the final version.

Competing Interests Statement

The authors declare no competing interests.

The cell cycle checkpoint machineries constitute important pathways that coordinate DNA damage and replication challenges with DNA repair and cell cycle progression. The initiating protein kinases ATM and ATR, yeast Tel1 and Mec1 respectively, show great promise as targets for drugs in anti-cancer treatment [1]. These two kinases play broad and complex regulatory roles, not just in situations of replication stress or DNA damage, but also during normal cell cycle progression. However, our current structural, biochemical, and mechanistic understanding of these enzymes remains poor, hindering our understanding of DNA damage response processes and effective therapeutic intervention.

Yeast Mec1 (hATR) belongs to the family of phosphatidylinositol-3- kinase-related kinases (PIKK), which also include yTel1 (hATM), yTor1, 2 (mTOR), and DNA-PKcs [2]. Both $Mec1^{ATR}$ and $Tel1^{ATM}$ show a basal protein kinase activity that is stimulated by specific activator proteins in response to DNA damage or replication stress [3-10]. Three activators have been identified, which stimulate Mec1 activity in a cell cycle specific manner[11,12] (Fig. 1a). Mec1 and its integral partner Ddc2 (hATRIP) exist in a stable complex as a dimer of heterodimers [13,14]. Ddc2 contributes to the stability of the complex through Ddc2-Ddc2 dimerization [15] and Ddc2-Mec1 interactions, and directs Mec1 to the site of damage through its direct interaction with the single-strand (ss) DNA binding protein RPA [16]. Ddc2 is also regulated by phosphorylation and its degradation contributes to checkpoint adaptation [17].

The kinase domains of PIKKs contain a number of highly conserved functional motifs found in almost all kinases; these include, a Glycine rich-loop (G-loop), catalytic loop that harbors residues responsible for Mg^{2+}-ATP binding, catalysis and phosphoryl transfer (e.g. the highly conserved HRD motif, which is DRH in PIKKs), and a Mg^{2+}- and peptide-binding activation loop that usually contains a DFG motif, with minor variability in PIKKs (DLG, DFD, DFN) (Fig. 1b,c). The DFG-Asp is invariant and responsible for chelating the magnesium required for catalysis [18]. The DFG-Phe is highly conserved, with the exception of $Tel1^{ATM}$ in which it is replaced by a Leu (Fig. 1c); while the Gly is replaced by an Asp in Mec1 or Asn in ATR. A distinct feature of the PIKK family is a region referred to as PRD (PIKK regulatory domain), which is thought to play a role in regulating the catalytic activity by mediating interactions with other proteins [5,19,20] and regulating protein substrate access [21]. PIKKs also have variable lengths of N-terminal HEAT repeats followed by a conserved FAT domain. Various roles for these additional domains have been elucidated in the last few years through structural and biochemical studies [22-24].

An integrated mutational analysis of $Mec1^{ATR}$ and PIKKs in general by both biochemical and genetic methodologies has been scarce. Point mutations in the Mec1 catalytic residues Asp2224 and Asp2243, which coordinate Mg^{2+}, show a phenotype similar to that of the *mec1Δ* mutant [25,26]. A point mutation in the PRD region of human ATR, Lys2589 (Lys2326 in Mec1) was shown to affect the activation by TopBP1 (the ortholog of yeast Dpb11) [5]. Recent cryoEM structures of Mec1-Ddc2 and ATR-ATRIP have revealed some of the key interactions [27,28]. However the structural models of Ddc2 and ATRIP were not fully resolved in those structures and there are a number of discrepancies between the cryoEM structure of Mec1-Ddc2 and that of the crystal structures of the domain containing the Ddc2 coiled-coil and RPA-interacting site [15,29]. Furthermore, these studies do not address how the kinase

activity of Mec1 is maintained in a basal state and what conformational changes are required to stimulate its activity.

The activation loop of PIKK kinases is widely conserved in eukaryotes. It shares homology with other protein kinases and can undergo large conformational changes when switching from inactive to active states [30]. In Mec1, the activation loop spans between residues H2241 and R2263, containing ^{2243}DFD^{2245} (Fig. 1c and Extended Data Fig. 1d). Close to the activation loop is a poorly conserved loop (^{2309}DRNMDHSIQ^{2317}), which is flanked by two α-helices. In a recent structural comparison of several PIKKs, including Mec1 and Tel1, this region has been designated PRD-I (PRD Insertion), which is proposed to be key in maintaining Tel1^{ATM} in an inhibited state through blocking substrate access [21]. Here, using an integrated biochemical and genetic analysis for checkpoint function, we identified a number of mutations in the activation loop and the PRD-I that have profound effects on its activity. Remarkably, we find that a single substitution in the DFD motif, F2244L, results in constitutive activity *in vitro*. This mutant can rescue the lethality of a yeast mutant deficient for all activators of Mec1. To corroborate these mutagenesis studies, we determined the structures of the AMP-PNP-bound form (a non-hydrolysable analog of ATP) of wild-type Mec1-Ddc2 and Mec1(F2244L)-Ddc2 by cryoEM at 3.8 Å and 2.8 Å resolution, respectively. Together, our results explain how Mec1-Ddc2 maintains minimal basal activity and the structural basis for its activation. Furthermore, these structures, together with our genetic and biochemical data, explain the unique property of the DFD motif and other key functional regions, and suggest a robust model of how Mec1^{ATR} is activated.

Results

The activation loop regulates Mec1 basal activity

We constructed, overproduced and purified 25 Mec1 point mutants that yielded homogeneous heterodimeric Mec1-Ddc2 complexes, similar to wild-type (see Methods). We compared the biochemical activities of these mutants with wild-type in terms of their basal protein kinase activity, and that of kinase stimulation by the activator Dpb11^{TopBP1}. Additionally, we used a second Mec1 activator, the nuclease-helicase Dna2, which is involved in DNA replication and DNA repair, but in addition has an S-phase specific replication checkpoint function, residing in its N-terminal domain (NTD;1-499) [31]. This Dna2 domain was used in order to query whether the Mec1 mutants showed defects that were dependent on the type of activator. Rad53 checkpoint kinase, the major target of Mec1 during checkpoint initiation, was used as the phosphorylation target. Basal Mec1 kinase assays (without activator) were carried out at both 40 and 100 mM NaCl to separate effects on nucleotide- and Mg^{2+}- binding, as higher salt is shown to eliminate weak Mg^{2+} binding [32]. All kinase assays with activator were carried out at 100 mM NaCl, which is the optimal salt concentration for wild-type Mec1 [6]. Using a complementary genetic analysis, we tested the equivalent *mec1* mutants for their effect on growth, sensitivity to the replication inhibitor hydroxyurea (HU) and to DNA damaging agents in several indicator strains that are progressively compromised for the cell cycle checkpoint circuitry.

We first targeted the activation loop for mutagenesis. Mutation of either H2241 or V2242, which are conserved in ATR and other PIKKs, led to a sharp reduction of Mec1 activity

(Fig. 2a-c). Mutation of D2243 to Asn was phenotypically similar to *mec1Δ* and the purified mutant showed no kinase activity, similar to previous reports [25,26]. We also targeted the highly conserved F2248 in the activation loop for mutagenesis. Mec1(F2248A) showed reduced basal activity and activation by Dpb11 (Fig. 2a-c).

To test the phenotypes of these mutants, we used a centromere plasmid shuffle technique to replace wild-type *MEC1* with each of the *mec1-x* mutants in a *mec1Δ* strain. In addition, we used progressively checkpoint-compromised strains, defective for the second checkpoint kinase Tel^{ATM} (*tel1Δ*), or in addition for Ddc1 (*tel1Δ ddc1Δ*). Ddc1 is a subunit of the 9-1-1 (Ddc1-Rad17-Mec3, human Rad9-Rad1-Hus1) checkpoint clamp [33,34]. In the *ddc1Δ* mutant, both the checkpoint functions of 9-1-1 and Dpb11 (human TopBP1) are defective [7], leaving only Dna2 as S-phase specific Mec1 activator [8].

The *mec1-H2241A*, *mec1-V2242A*, and *mec1-F2248A* mutants, which showed 70-90% reduction in kinase activity, showed defects under unchallenged growth conditions, and sensitivity to growth on hydroxyurea. These strains showed exquisite sensitivity to hydroxyurea when the checkpoint circuitry was progressively compromised in the *tel1Δ* and *tel1Δ ddc1Δ* genetic background (Fig. 2d), thus establishing a direct correlation between *in vitro* kinase activity and *in vivo* growth and hydroxyurea-sensitivity.

A surprising function of F2244 in the DFD motif

Central in the activation loop is the highly conserved F2244 of DFD, which we mutated to Ala, and also Leu because Tel1^{ATM} has Leu at that position (Fig. 1c). F2244A and F2244L Mec1-Ddc2 proteins showed unusual high basal activity, ~10-fold and ~20 fold higher for the F→A and F→L mutant, respectively. For our further studies, we selected Mec1(F2244L), which showed the highest basal activity at 100 mM NaCl and only minimal activation by Mec1 activators. Indeed, activation of Mec1(F2244L) by Dpb11 and Dna2(1-499) or a small peptide derived from Dna2 [8], was less than 1.5 fold (Fig. 2a-c and Extended Data Fig. 1b,c). However, the fully activated mutant enzyme showed only half the activity of activated wild-type Mec1 (Fig. 2b). In a control assay, we showed that the increase in basal activity was not due to an enhanced affinity of the mutant enzyme for the substrate, Rad53 (Extended Data Fig. 1e).

We replaced *MEC1* with the constitutive active allele *mec1-F2244L*. In wild-type yeast, this mutation exhibited slow growth (Fig. 2d, top panels). Interestingly, in the checkpoint-compromised *tel1Δ ddc1Δ* mutant background, *mec1-F2244L* showed slightly increased growth over wild-type on 100 mM hydroxyurea (Fig. 2d, bottom panels). The poor growth of *mec1-F2244L* in wild-type yeast could be due to gratuitous, damage-independent phosphorylation of key cell-cycle factors, which can affect progression of the cell cycle. Indeed, a FACS analysis of the mutant shows that it progressed more slowly through S-phase (Extended Data Fig. 2d). Surprisingly, *mec1-F2244L* showed little or no increased phosphorylation of Rad53, the major downstream effector in DDR and replication stress, unless cells were challenged with DNA damage or hydroxyurea (Fig. 2e)[35-37]. Thus, it appears that slow growth of the mutant is not caused by gratuitous, canonical checkpoint activation. To investigate another possible target of *mec1-F2244L*, we probed the phosphorylation status of histone H2A. S129 of H2A is a target for Mec1, and its

phosphomimetic mutant S129E facilitates DNA repair [38,39]. Treatment of synchronized wild-type S phase cells with hydroxyurea resulted in transient phosphorylation of H2A, being high after 30 min, but largely abolished after 60 min [40] (Extended Data Fig. 2a). To eliminate possible contributions to the phosphorylation signal by Tel1, we repeated this experiment in *tel1Δ*, with comparable results (Fig. 2e). Remarkably, the *mec1-F2244L* mutant showed constitutive phosphorylation of H2A in all phases of the cell cycle. Treatment with the DNA damaging agent 4-nitroquinoline 1-oxide (4NQO) resulted in robust phosphorylation of *MEC1* cells also in G1 and G2 (Fig. 2e).

Constitutively active *mec1-F2244L* replaces the need for Mec1 checkpoint activators

A minimally active checkpoint is important for the viability of yeast. Cells that are *tel1Δ*, but wild-type for *MEC1* show extreme growth defects and massive genome instability when all three activation mechanisms for Mec1 are eliminated in strain *MEC1 tel1Δ ddc1Δ dna2-WY128,130AA* [8,41]. The double point mutations in *DNA2* eliminate its checkpoint activity without compromising its essential DNA replication and repair functions. *Mec1-F2244L* but not a second copy of wild-type *MEC1* restored robust growth of the activator-deficient mutant in a dominant manner (Fig. 2f and Extended Data Fig. 2b). This strain is also moderately resistant to DNA damage and replication stress (Fig. 2f).

Consistent with previous results [8], the activator-deficient strain is defective for phosphorylation of both H2A and Rad53 in response to damage or stress (Fig. 2g, lanes 1-4). On the other hand, damage-dependent phosphorylation of both targets is restored with *mec1-F2244L* (lanes 5-8). While significant H2A phosphorylation is observed without DNA damage, it is enhanced by 4NQO treatment, indicating that localization of the constitutively active Mec1-F2244L to stalled forks or DNA repair intermediates enhances its activity. As shown before in Fig. 2e, full phosphorylation response of Rad53 requires DNA damage.

Overview of the structures of Mec1-Ddc2 and Mec1(F2244L)-Ddc2

Our data suggest that Mec1(F2244L) mimics the activated state, which rescues activator-defective cell growth and confers increased DNA repair functionality. In order to provide a molecular basis for its constitutive activity, we determined the Mec1(F2244L)-Ddc2 structure to 2.8 Å and a wild-type structure to 3.8 Å resolution, both in the presence of Mg^{2+}-AMP-PNP to mimic pre-catalysis state (Fig. 3a,b, Extended Data Fig. 3, Extended Data Fig. 4 and Extended Data Fig. 5). We also obtained a structure of wild-type in an apo form at lower resolution (4.3 Å), and its features are broadly similar to that of the nucleotide-bound form at this resolution (Extended Data Fig. 3 and Extended Data Fig. 4). The high-quality cryoEM 3D reconstruction of the Mec1(F2244L)-Ddc2 Mg^{2+}-AMP-PNP-bound complex allowed us to unambiguously assign and build an atomic model for the entire Mec1 protein (residues 2-2368) and Ddc2 from residue 187 to the C-terminus (residue 747) (Fig. 3a-d). We assign a series of regions in Mec1 that are structurally related to the previously assigned domains of PIKKs [21], denoted as N-HEAT, C-HEAT, Bridge, N-FAT, M-FAT, C-FAT, and Kinase (Fig. 3a-c). This model was fitted, refined and rebuilt into wild-type maps, which are of lower resolution possibly due to intrinsic flexibility (Extended Data Fig. 4). We also observe a CCHC-type Zinc finger (residues C467, C490, C493, H553)

within the Mec1 N-HEAT domain, that likely performs a structural role to stabilize the interaction with Ddc2 (Fig. 3e).

Our structural model of Ddc2 and Mec1 NTDs differs substantially from a previously determined structure [27] (Extended Data Fig. 6 and Extended Data Fig. 7). In our model, Mec1 NTD is well-structured (Extended Data Fig. 6), forming a HEAT solenoid (termed N-HEAT) that cradles Ddc2 with a buried surface of nearly 7000 $Å^2$ (Fig. 3d). This is consistent with earlier data showing that Ddc2 interacts with ~600 N-terminal residues of Mec1 [42]. In the previously published structural model, the first 200 amino acids of Mec1 were missing and instead this part was assigned as the Ddc2 NTD (Extended Data Fig. 6 and Extended Data Fig. 7), in stark contrast to the crystal structure and biochemical data showing that Ddc2 NTD possesses a coiled-coil domain, forming an elongated dimer, and an RPA-interacting domain [15,29]. The Ddc2 NTD is missing in our 3D reconstruction despite the use of full-length proteins, presumably due to these domains being flexibly tethered to the rest of Ddc2 by an ~50 amino acid linker. Our model thus reconciles and supports previous crystal structures, and models based on biochemical analysis. Our new Ddc2 structural model shows that two of the Mec1-dependent phosphorylation sites of Ddc2 (T29, T40) [17] and the reported DNA-binding region (177-180) would be accessible [43].

Both wild-type and F2244L Mec1-Ddc2 form a dimer of heterodimers, as reported previously [13]. The dimer interface is comprised of 3 layers; two are exclusively formed by the Mec1 dimer, with the kinase domain and C-FAT forming an upper layer, and M-FAT forming the middle layer. The lower layer is exclusively formed by the Ddc2 homodimer (Fig. 4a,b). Comparisons between the wild-type and F2244L structures show that dimer interfaces mediated by Ddc2 and M-FAT are largely unchanged, whereas the dimer interface formed by the kinase and C-FAT domain differ significantly (Fig. 4c-e). In the F2244L structure, an ~15° rotation of the kinase domains around the C2 axis was observed, which shifts the kinase domains away from one another by up to 10 Å (Fig. 4b,c), altering the dimer interface (Fig. 4d,e). This displacement of the kinase domains is concomitant with a clockwise motion of the C-FAT relative to the kinase C-lobe (Fig. 4f) and kinase N-lobe motion (Fig. 4g and Supplementary Video 1). Further, the PRD-I in the F2244L mutant moves away from the nucleotide-binding pocket towards the dimer interface by up to 10 Å, retracting from the active site via a loop to helix transition (Fig. 4g).

Conformational changes near the nucleotide-binding pocket reveal key regions for auto-inhibition and activation

In the wild-type structure, the triphosphate moiety of the bound nucleotide is too distant from the catalytic residues to allow robust activity (Fig.5a). The catalytic loops in the wild-type and mutant structures remain largely unchanged (Fig. 4g and Fig. 5a,b). However, in the activated state, represented by Mec1(F2244L), the kinase N-lobe moves inwards, causing closure of the nucleotide binding site (Fig. 4g and Fig. 5a,b and Supplementary Video 2). The nucleotide is moved ~2-3 Å towards the catalytic center and is now correctly presented to the DRH motif (mirrored HRD, Fig. 5a,b). Furthermore, the G-loop moves ~5 Å towards the nucleotide, enabling hydrogen bonding of the invariant S2058 with the β−γ phosphates of AMP-PNP (Fig. 5c), as observed in mTOR [20]. In addition to the G-loop, the N-lobe

contributes to nucleotide binding via hydrophobic interactions around the adenine ring, including M2078 (the so-called gatekeeper residue), and via an invariant K2080 hydrogen bonding with α–β phosphate (Fig. 5c).

Two highly similar conformations were obtained within the Mec1(F2244L) dataset, with one at 2.8 Å (State I) and the second at 3.2 Å (State II). Differences between these two activated states center around the D[F/L]D motif (Fig. 5c-f). While D2243, which coordinates both Mg^{2+}, remains largely unchanged, F2244L 'wobbles' in its hydrophobic pocket (Fig. 5c,e). Critically, D2245 coordinates the 2^{nd} Mg^{2+} in both states (Fig. 5c-f), suggesting a critical role for this motif in Mec1. However, the rotamer conformation of State II D2245 also allows E2082 to interact with the catalytically essential K2080 (Fig. 5e, equivalent to the E91:K72 salt bridge in protein kinase A, a hallmark of an active state [44]). Additional contacts between main chain of the D[F/L]D motif and side chains of D2087 and Q2086 are also observed (Fig. 5e). The extensive network of H-bonds that stabilizes the activation loop suggests that State II might represent a more active configuration.

The non-canonical DFD motif of Mec1 plays a critical role in kinase activity

The remarkable properties of F2244 highlight its critical role in kinase activity and are corroborated by the structures (Fig. 6a,b). The differences in activity between wild-type and Mec1(F2244L) could be manifold, for example: nucleotide binding, hydrolysis, or phosphoryl transfer. We carried out a comparative ATPase analysis of wild-type and Mec1(F2244L), in the presence or absence of Rad53 substrate and Dna2 activator (Fig. 6c). We performed identical assays with either α–^{32}P-ATP (total ADP formed) or γ–^{32}P-ATP (substrate phosphorylated) to determine whether ADP formation was productive (phosphate transfer to protein substrate) or unproductive (transfer to water). Wild-type Mec1 showed very low ATP turnover and kinase activity, unless Dna2 activator was present (Fig. 6c). Dna2 and Rad53 increased the ATPase 12-fold. Importantly, all ATP used is coupled to phosphoryl transfer to Rad53. However, in the absence of the Rad53, Dna2 caused an increase in unproductive hydrolysis. In contrast, the ATPase activity of Mec1(F2244L) alone is already ~14 fold higher than wild-type. This is consistent with structural data showing that its nucleotide binding site and all catalytic residues are properly assembled (Fig. 5c,e). With Rad53 substrate present, the increased ATP turnover is poorly coupled to kinase activity (Fig. 6c). This could be due to the altered environment of the mutant, which may still retain water in the active site for unproductive transfer [45]. Similar results were obtained with Dpb11 as activator, although the analysis was more complicated because Dpb11 is also a Mec1 substrate (Extended Data Fig. 8c).

We also carried out an ATP concentration dependence of kinase activity to determine binding affinity. The apparent ATP Km for Mec1(F2244L) is ~5 fold lower than that for wild-type in the absence of activators (Extended Data Fig. 8a,b), suggesting that activated form, via activator binding or constitutive active mutant, promotes ATP binding. These results are consistent with the structures. In the wild-type protein without activator, the G-loop is further away from the catalytic center, resulting in an ATP binding pocket with lower affinity (Fig. 5a,b and Fig. 6a,b). These data indicate that the increased activity in F2244L is due to enhanced nucleotide binding and hydrolysis.

To understand why the F2244L mutation induces such dramatic changes, we examined the environment surrounding F2244. Mutant L2244 is inserted in a hydrophobic pocket formed by Y2117, Y2090 and M2091 of the KαC and L2247 of the activation loop (Fig. 6b). Disrupting these interactions by substituting F2244 with a charged residue (F2244K or F2244D), eliminated all kinase activity (Fig. 6d,e), and the mutants were unable to complement lethality of *mec1Δ* (Extended Data Fig. 8d). Mutation to the small hydrophobic Ala yielded a lower activity enzyme than F→L (Fig. 6d,e), probably due to increased flexibility of the activation loop. Given these considerations, a larger hydrophobic residue could stabilize the active state. Indeed, while at 100 mM NaCl, the basal activities of both Mec1(F2244W) and Mec1(F2244Y) were like wild-type, the mutants showed increased apparent affinity for Dpb11 and higher stimulated activity (Fig. 6e). Furthermore, while the aromatic substitutions are phenotypically silent in a wild-type (not shown) or *tel1Δ* strain, they showed an increased resistance to hydroxyurea in the checkpoint-compromised *tel1Δ ddc1Δ* strain (Fig. 6f).

While both the F2244L and the F2244W/Y mutants show hyperactivity, they are mechanistically distinct. Mec1 activation requires relief of the inhibition state and establishment of the active site. In the simplest interpretation of this model, Mec1 is in a two-state equilibrium between inhibited and activated state, which is normally regulated by Dpb11 (or another activator). The F2244W/Y mutants have low basal activity like wild-type (Fig. 6d), suggesting that they are largely in the inhibited state without activator, but they have a lower energy barrier for Dpb11-mediated transition to the activated state. Therefore, these mutants are phenotypically silent in a checkpoint-proficient strain. In contrast, for F2244L, the equilibrium between the inhibited and activated state is strongly shifted to that of the activated state in the absence of activator, hence the growth defect of *mec1-F2244L* in a checkpoint-proficient strain due to elevated Mec1 activity. On the other hand, in checkpoint compromised *tel1Δ ddc1Δ*, the F2244L mutant shows increased resistance to hydroxyurea because of its constitutive activity, whereas the F2244W/Y mutants show increased resistance because a lower level of activator suffices for a robust response.

Changing the DFD motif to DFG, the canonical motif for most protein kinases, highlights the importance of the Mg^{2+} chelation function of Mec1 D2245. Mec1(D2245G) showed a significant decrease in the apparent affinity for Dpb11, and a decreased basal activity (Fig. 6g,h). The mutant showed strong defects when tested in a checkpoint-compromised background (*tel1Δ ddc1Δ*) (Fig. 6i). When the central motif was mutated to DLG, the motif found in $Tel1^{ATM}$, a robust response to Dpb11 was restored (Fig. 6h), and the double mutant showed no phenotype (Fig. 6i), suggesting that the defects caused by D2245G are rescued by F2244L. Remarkably, among the variations in this motif observed in 640 $Mec1^{ATR}$ species, there is not a single occurrence of the DLD motif, which causes constitutive activity (Extended Data Fig. 1d). Mutations in this motif are also not found in the cancer mutation databases.

The Mec1 PRD-I prohibits an active conformation of the activation loop

The PRD-I is a poorly conserved element between Kα9 and Kα10, and ranges in length from 6-9 amino acids in $Mec1^{ATR}$, 43-50 in $Tel1^{ATM}$, and >70 residues in mTORC1 [46]. In

Tel1^{ATM}, PRD-I coincides with the putative substrate-binding site, acting as an auto-inhibitory element [21]. While substrate competition is a clear role for the PRD-I in Tel1^{ATM} and other PIKKs, the PRD-I in Mec1 is only a short connecting linker (^{2309}DRNMDHSIQ^{2317}).

Wild-type Mec1 does not adopt a defined DFD conformation (Fig. 6a and Extended Data Fig. 9a-c). This is consistent with the wide range of DFG configurations that render kinases inactive but limited conformations that enable activity [44,46,47]. Nevertheless, our structural data suggest a hydrophobic network between PRD-I and the activation loop in the inactive state (Fig. 7a). In the activated state, PRD-I moves away from the activation loop and undergoes a loop to helix transition, shortening the loop between Kα9 and Kα10 (Fig. 4g and Fig. 7a-c and Supplementary Video 3). The retraction of PRD-I from the activation loop upon activation suggests that PRD-I may also play an auto-inhibitory function in Mec1. To further understand the role of PRD-I, we mutated several residues (Fig. 7d-f). In the wild-type structure, M2312 sits above the highly conserved F2248, similar to W2701 in the Tel1 PRD-I (Fig. 7a and Extended Data Fig. 9d,e). D2313 and H2314 form putative interactions with R2253 and E2249 of the activation loop. M2312A and H2314A mutations, which likely perturb PRD-I/activation loop interactions, indeed showed modestly increased basal- and Dpb11-stimulated activity (Fig. 7d,e). D2313 may stabilize the activated states. In State I, it interacts with H2314 in the newly formed helix, suggesting it could aid the loop-to-helix transition of the PRD-I (Fig. 7b). In State II, D2313 moves inwards, coinciding and possibly assisting with M2312 flipping out (Fig. 7c). Remarkably, the D2313A mutation showed strongly reduced basal and activated kinase activity (Fig. 7d,e), suggesting an important role in PRD-I re-arrangement during activation. Even though R2310 undergoes a large rotation upon activation (Fig. 7b), the R2310A mutation, showing slightly reduced activity, was less informative. The differences in biochemical activity of these PRD-I mutants are reflected in their phenotypes in yeast. In the checkpoint-compromised strain (*tel1Δ ddc1Δ*), the *mec1-M2312A* and *mec1-H2314A* mutants with increased biochemical activity were more resistant to hydroxyurea than wild-type (Fig. 7f). An explanation for the increased resistance is the same as proposed above for the F2244W/Y mutants.

A pocket in the activation loop-interacting helix KαC docks F2244 in the active state

The motion of the KαC, which directly contacts the activation loop and the PRD, may couple the activation loop conformation with the release of the PRD-I. M2091 and F2093 are highly conserved residues in this network. Alanine mutation of M2091, which forms part of the hydrophobic pocket in which F2244 is predicted to sit when activated (Fig. 6a,b), behaved similarly to wild-type (Fig. 7g-i). This mutation may be tolerated because Y2117 and Y2090 are still able to wedge F2244 in its correct position. On the other hand, mutation of F2093, which is sandwiched between L2299 of Kα9 (PRD) and L2220, adjacent to the catalytic loop, showed low basal kinase activity and a strong defect in activation by Dpb11 (Fig. 7g,h). Comparison between the activated and inactive structures show that the F2093A mutation would disturb the packing of the Kα9 and KαC such that it may become more difficult to fully activate, thereby explaining the Dpb11-mediated stimulation defects (Fig. 7a-c), and compromised growth in a *tel1Δ* mutant and extreme hydroxyurea sensitivity (Fig. 7i).

Discussion

In this work, we present an integrated analysis of key functional regions in Mec1^{ATR} to unravel the complex regulatory network that governs its low basal activity and activation, and the requirement of kinase activity and activators in normal growth and response to damage or replication stress. Constitutive activity of Mec1(F2244L) was marked by poor yeast growth, likely by increased phosphorylation of cell cycle targets. We detected high, constitutive phosphorylation of histone H2A (the yeast form of γ-H2AX), a hallmark of DNA repair (Fig. 2e) [38,39]. When the checkpoint circuitry is compromised because of Mec1 activator loss, 9-1-1, Dpb11, and Dna2 (Fig. 2f,g), the constitutive mutant rescues the growth phenotype, indicating that there is an optimal window of Mec1 activity for cell cycle progression and growth.

A two-pronged activation mechanism reverses inhibition by PRD-I and reconfigures the activation loop

Our data indicate that the PRD-I is a key regulatory element, by holding the activation loop in an inactive conformation through a network of weakly-held interactions. The inhibition can be released through mutagenesis or by activator binding, resulting in stimulation of basal kinase activity. F2244 is critical for both the auto-inhibited and activated states, reminiscent of the DFG-in/out activation mechanism in many kinases [47,48]. Altered basal and stimulated activity are observed when the DFD Phe is substituted for either larger (Trp or Tyr) or smaller (Leu or Ala) hydrophobic residues. Interestingly, Mnks (MAP kinase-interacting kinases) also possess a non-canonical DFD motif with the Phe placed in an auto-inhibited conformation in the absence of activators [49].

Our studies suggest that Mec1 activation requires 1) the removal of the inhibition imposed by PRD-I and 2) the establishment of the activated state. The two requirements are interconnected with the relocation of PRD-I coupled to conformational changes in C-FAT and N-lobe, which contribute to the active site reconfiguration. This two-pronged mechanism is reflected in the highly complex behavior of many of the mutants, as many regions, e.g. the activation loop and PRD-I, are involved in both maintaining auto-inhibition and establishing activation. Within PIKKs, a C-FAT rotation and N-lobe closure were also proposed for DNA-PKcs, mTORC1 and ATM^{Tel1}, via allosteric conformational changes upon activator binding, which is remote from the kinase domain [22-24,50,51]. It thus seems that C-FAT rotation and N-lobe movement may be conserved features in all PIKKs irrespective of the activator binding site or exact activation mode. Mec1 employs an activation mechanism that contains elements operating in mTORC1 (FAT and N-lobe movement), and kinases using a DFG-in/out mechanism. Whether these features are shared by other PIKKs remains to be determined.

The unique DFD/N in Mec1^{ATR} is associated with its distinctive activation mechanism

The unique activation mechanism we unraveled here centers around the DFD motif. Indeed, although the majority of PIKKs possess a canonical DFG motif, mutating the DFD motif to DFG resulted in an incapacitated kinase. Our structures suggest that this is due to differences in Mg^{2+} coordination. Unlike in other PIKKs, in Mec1, 2nd Mg^{2+} coordination is stabilized

by the 2nd aspartate of its DFD motif (Fig. 5c-f and Extended Data Fig. 9f-i), and likely also by the asparagine of the more common DFN motif, and this does not require substrate binding. This is indeed consistent with the observation that the activated form of wild-type Mec1 can hydrolyze ATP in the absence of substrate, and the F2244L mutant can achieve maximum ATPase activity without substrate or activator (Fig. 6c). In many other kinases, 2nd Mg^{2+} coordination involves substrate binding. In some kinases, such as CDK2 and PKA, the second Mg^{2+} binding is shown to be the final, rate-limiting step in catalysis [45,52]. The differences in 2nd Mg^{2+} coordination might thus reflect differences in the rate limiting step among PIKKs, be it substrate binding or establishing the active site, as observed for Mec1.

Methods

Yeast strains, plasmids and proteins

Yeast strains used in this study were prepared using PCR based methods for gene disruption in which marker cassettes flanked by 100-200 bp of regions homologous to the targeted gene were synthesized and used to transform C10-2A strain (W303 *RAD5*) [53] for genomic integration. *S. cerevisiae MEC1* is an essential gene, however, the lethality of *mec1Δ* mutants is rescued by deletion of the ribonucleotide reductase inhibitor *SML1* [54,55]. In our genetic analysis, we have used strains that are *SML1* wild-type. PY405 (MATa *ade2-1 can1-100 his3-11,15 leu2-3,112 trp1-1 ura3-1 mec1Δ::KanMX* containing pGM004 (*MEC1 URA3*)) was derived from C10-2A. Integration of *tel1Δ::NAT* in PY405 yielded PY406, and further integration of *ddc1Δ::HIS3* yielded strain PY414.The complementing plasmid pGM004 contains the *MEC1* gene on a centromeric plasmid under control of its own promoter, with *URA3* as both selectable and counterselectable (on 5-fluoroorotic acid, 5FOA) marker [17]. Transformants were selected on YPD plates containing the respective drug and verified by PCR analysis.

PY270 (MATa *can1 his3-Δ200 leu2 trp1 ura3-52 dna2Δ::HIS3 ddc1Δ::KanMX4 tel1Δ::NAT*—*pBL583*** (*MEC1 URA3*)) was described previously [8]. For each of the Mec1 mutants, we generated a centromere plasmid: p(*mec1-x LEU2*) is pBL905-x (*mec1-x ARS1 CEN4 LEU2*) for genetic analysis [26]. A 2-micron plasmid pBL904-x (2 μm ori *TRP1 mec1-x DDC2*), with the *mec1-x* and *DDC2* genes placed under control of the galactose-inducible *GAL1-10* promotor, was used for overproduction of the Mec1-Ddc2 complex [13]. *MEC1* mutants were made using standard methodology and all mutants were verified by DNA sequencing. Other plasmids have been described previously [8]. Purification of Dpb11 and Dna2(1-499) was as described [8].

Purification of Mec1 mutants

Strain PY252 (MATα *can1 his3 leu2 trp1 ura3 GAL pep4Δ::HIS3 nam7Δ::KANMX4 mec1Δ::KANMX6 sml1Δ::HYG*) was used to overexpress Mec1 or Mec1 mutants from the plasmid pBL904-x series, essentially as described [13], with some modifications. After galactose induction of 12 liters of growth culture, cells were harvested, lysed and subjected to affinity purification on IgG beads (2 ml). After extensive washing steps, the protein was eluted from the column by overnight incubation with HRV-3C protease at 4 ˚C. After

elution, the Mec1 preparations were stabilized with 1 M final trimethylamine N-oxide prior to freezing and storage.

Mec1 Kinase assay

Throughout this study, we used the kinase-dead version (K227A) of Rad53, fused to the Glutathione-S-transferase (GST) purification tag (GST-Rad53-kd), as substrate for Mec1 kinase. Phosphorylation of 600 nM Rad53, or as indicated, was performed in a 10 μl assay containing 25 mM Hepes-NaOH pH 7.4, 2 % glycerol, 1 mM DTT, 20 μg/ml BSA, 0.08 % ampholytes pH 3.5-10, 8 mM Mg-acetate, 100 μM ATP, 0.5 μCi [γ $-^{32}$P] ATP or as indicated, 40 or 100 mM NaCl final concentration (including contributions made by protein storage buffers), and 3 nM Mec1. Reactions were initiated by adding the indicated concentrations of Dpb11, Dna2-499, or Dna2-1 peptide [8], and incubated at 30 °C for 10 minutes. Reactions were quenched by adding 5 μl of 2.5x SDS-PAGE loading dye and heated at 95°C. Samples were separated on 8 % SDS-PAGE gel, dried, and exposed to phosphor screen (GE healthcare) and imaged with a phosphoimager. The bands were quantified using ImageQuant and plotted using KaleidaGraph. The activity of the Mec1 mutants was evaluated with respect to wild-type Mec1, overexpressed and purified analogously. Most assays were carried out in triplicate and the error bars in the Figures are standard error of the mean (s.e.m). Assays with mutants with low or no activity were carried out in duplicate and the plots show the average without error bars.

Mec1 ATPase

The assay was carried out essentially as described above in assay buffer with 100 mM NaCl and 100 μM of [α–^{32}P], and 200 nM Dna2-499 and 600 nM GST-Rad53-kd, where indicated. The concentration of Mec1 or Mec1-F2244L was raised to 10 nM to achieve significant formation of ADP. Aliquots were processed and the data quantified essentially as described [56]. A maximum of 15% ATP hydrolysis was observed. For the experiment in Fig. 6c and Extended Data Fig. 8c, this experiment was matched exactly with a substitution of [α–^{32}P] by [γ $-^{32}$P] ATP, and protein phosphorylation (Rad53 plus Dna2-499 or Dpb11) quantified.

Yeast cell growth and analysis

Standard media were used for yeast cell growth. Yeast strains PY405, PY406, and PY414 were transformed with plasmid pBL905 or its derivatives and selected on synthetic complete selection media, SC-Ura-Leu plates. Transformants were grown overnight in SC-Leu medium, and plated on SC-Leu plates containing 5-fluoroorotic acid (5FOA) to allow growth only of cells that had lost plasmid pGM004 (*URA3 MEC1*). These strains were grown overnight in SC-Leu medium and 10-fold serial dilutions spotted onto YPD plates, with or without hydroxyurea as indicated. Plates were incubated at 30 ˚C for varying times and photographed.

Yeast cell synchronization and FACS analysis was essentially carried out as described [57]. 200 mM hydroxyurea or 2 μg/ml 4NQO (4-nitroquinoline N-oxide) were added as indicated in the Figures. For Western analysis, the antibodies used were anti-Rad53 (ab104232; RRID:AB_2687603) and anti-histone H2A (phospho S129, ab15083; RRID:AB_301630)

antibodies, both from Abcam, at 1:2,000 and 1:500 dilution, respectively. The Rad53 antibody recognizes both unphosphorylated and phosho-Rad53, whereas the ab15083 antibody only recognizes phospho-H2A. Rad53 blots were developed using anti-rabbit IgG-alkaline phosphatase conjugated secondary antibody (Sigma A3687) at 1:10,000 dilution and imaged using a Typhoon phosphoimager in the fluorescence mode. H2A blots were developed using anti-rabbit IgG HRP-linked secondary antibody (Cell Signaling 7074S) at 1:2,000 dilution in 5% fat free milk prepared in TBST and analyzed using a Thermo Scientific myECL CCD digital imager.

Electron Microscopy Grid Preparation

A frozen aliquot of purified *Saccharomyces cerevisiae* $Mec1^{WT}$-Ddc2 or Mec1(F2244L)-Ddc2 was diluted using sequential addition of 10 μl volumes of buffer (50 mM Tris-HCl, 50 mM NaCl, pH 7.4, supplemented with AMP-PNP and Magnesium Acetate), and was incubated for 30 minutes on ice. The final concentrations of samples were as follows; Mec1-Ddc2 (apo), ~100nM; Mec1-Ddc2:AMP-PNP ~100 nM, 5 mM AMP-PNP, 10 mM $Mg(OAc)_2$; and Mec1(F2244L)-Ddc2:AMPPNP, ~80 nM, 2 mM AMP-PNP, 5 mM $Mg(OAc)_2$. Approximately 4 μl of the sample were deposited onto Lacey Carbon 300 mesh gold grids that also have an additional ultrathin carbon support layer (Ted Pella Inc. USA), which were plasma-cleaned for 20-30 seconds in air prior to sample application. Samples were vitrified by plunge freezing in liquid ethane at liquid nitrogen temperature using a Vitrobot Mk IV (FEI) set with a blotting force of −6, a waiting time of 60 s and a blotting time of 2 seconds, 4°C and 95% humidity.

CryoEM data acquisition

High-resolution movies were collected for Mec1-Ddc2 (apo), Mec1-Ddc2:AMP-PNP, and Mec1(F2244L)-Ddc2 on a Titan KRIOS (Thermo Fisher) at either the Francis Crick Institute (London, UK), or eBIC (Oxfordshire, UK). For all datasets, the microscopes were operated at 300kV with the specimen at cryogenic temperatures (approximately −180°C) with images recorded at 1-3 μm underfocus. Data for Mec1-Ddc2 (apo) was acquired on a Falcon III direct electron detector in linear mode at a nominal magnification of 75,000 X, corresponding to a pixel size of 1.09 Å, and a cumulative total electron dose of 59 $e^{-}/Å^2$. It was also necessary to collect a significant fraction of the data using a stage tilt of −30°. A total of 15097 micrographs (9214 tilted and 5833 untilted), fractionated into 11 frames, were collected. Data for Mec1-Ddc2:AMP-PNP and Mec1(F2244L)-Ddc2:AMP-PNP were acquired on a K3 direct electron detector (Gatan) with energy filter in super resolution mode at a nominal magnification of 81,000 X, corresponding to a calibrated pixel size of 1.06 Å (super resolution pixel size of 0.53 Å). For the Mec1-Ddc2:AMP-PNP grid, a total of 20185 micrographs, fractionated into 40 frames and with a cumulative total electron dose of ~43.6 $e^{-}/Å^2$. In the case of the Mec1(F2244L)-Ddc2:AMP-PNP mutant dataset, 15902 micrographs with a cumulative electron dose of 51 $e^{-}/Å^2$ were collected and fractionated into 50 frames.

CryoEM image processing apo dataset

Movie frames were aligned, corrected for drift, beam induced motion and dose-weighted using MotionCor2 [58] implemented in RELION-3.0 [59]. To estimate the contrast transfer

function (CTF) gradient across a tilted micrograph, local CTF fitting was performed using Gctf [60]. Particles were picked with Gautomatch using re-projections of a low resolution Mec1-Ddc2 EM structure [13,14] filtered to 30 Å. Particles were extracted in RELION-3.0 using a box size of 380 × 380 pixels and binned four times for initial processing. Due to the preferential orientation, specific views were low in number and therefore in order to keep these 2D classification was omitted as a first step. Instead 3D classification was performed with an initial Mec1-Ddc2 model [13,14], filtered to 60 Å. Initial 3D classification with 4 classes produced a single class (27% particles) that exhibited shape and features expected for this protein. Particles belonging to this 3D class were re-extracted, and twice binned before an initial consensus 3D refinement (C1), was performed, which converged to 5.3 Å. After 3D refinement the particle stack was further separated using 3D classification in RELION-3.0 using the consensus map filtered to 30 Å as a model and using local angular searches and higher T values (T=8), sub-dividing into a further four classes. Of the 4 classes several displayed over-fitted and noisy or broken features, however a single class (39% of the input particles) showed clear secondary structure and internal features and were selected for further refinement. Particles corresponding to the best 3D classes were re-extracted (1.09 Å/pixel) and the remaining poor particles removed using 2D classification without alignment. The best classes were selected resulting in a final particle stack of 132193 images, which were refined applying C2 symmetry in RELION-3.0, according to the gold-standard refinement procedure. Beam-induced Bayesian particle polishing [61] followed by CTF refinement [59] was also performed, producing a final map of the Mec1-Ddc2 at 4.7 Å, according to the FSC = 0.143 criterion, after post processing in RELION-3.0 using a soft mask (C2 symmetric) corresponding to the protein. Auto-refinement of the same particles in cisTEM [62], using the 4.7 Å reconstruction filtered to 20 Å as a starting model, produces a 4.3 Å map with features consistent with such estimates. The reconstructed volume was slightly larger than that obtained for the wild-type bound with nucleotide (see below), suggesting an inaccurate pixel size. Therefore, the volume was scaled to match the volume of the nucleotide-bound reconstruction, with a pixel size of 1.05 Å/pixel producing a closely matched structure. The numbers of particles and processing steps are summarized in Extended Data Fig. 3. Local resolution estimates calculated using ResMap [63] showed a resolution range of 3.5 Å – 5.5 Å. Angular distribution plots suggest, while there are predominant views, rare views were captured by omitting initial 2D classification steps and tilting also circumvented the severity of the preferential orientation issues as confirmed by directional FSC plots [64].

CryoEM Image Processing of AMP-PNP-bound WT and F2244L datasets

Movie frames were process analogously to the wild-type dataset except that the super resolution images were twice binned, and gain corrected as part of the MotionCor2 processing step in RELION-3.0. Contrast transfer function (CTF) fitting was performed using CTFFIND4 [65]. Particles were picked with Gautomatch using the same templates as for the wild-type dataset and extracted using RELION-3.0 with a box size of 328 × 328 pixels and down sampled 4 times for initial processing. Again, 3D classification was initially performed with a Mec1-Ddc2 map [13,14] filtered to 60 Å. Data processing for Mec1-Ddc2:AMP-PNP followed a similar pipeline to that described for the apo structure (above), and also exhibited preferential orientation. However, careful classification using 2D and 3D

approaches in RELION-3.0 were used to balance the views to counter the preferential orientation and to prevent anisotropic reconstructions that were difficult to interpret. Due to the relatively rare high-resolution front views (those that are described as butterfly in shape), the number of particles used in the final reconstruction was comparatively low compared to the dataset size. These particles were subjected to particle polishing and CTF refinement in RELION-3.0, resulting in a 4 Å resolution reconstruction when refined in RELION-3.0 according to the gold-standard refinement procedure and applying C2 symmetry. Auto-refinement of the same particle stack in cisTEM, using the a 20 Å filtered map as a starting model, produces a 3.8 Å reconstruction (FSC = 0.143). The numbers of particles and processing steps are summarized in Extended Data Fig. 3. Local resolution estimates were calculated using ResMap [63] and showed a resolution range of 3.5 Å – 4.5 Å. Angular distribution plots suggest, while there are predominant views, carefully curating the particle stack maintained the rare views.

The Mec1(F2244L)-Ddc2:AMP-PNP data were preprocessed as described above (summarized in Extended Data Fig. 5). Initial 3D classification with 4 classes produced a single good class (47% particles). Particles belonging to this good 3D class were re-extracted, twice binned, and used in a consensus 3D refinement (C1) that converged to 4.3 Å. A 3D classification in RELION-3.0, using local angular searches with a starting map filtered to 30 Å and separating into 4 classes, produced a single main class (52%) exhibiting clear secondary structure features. Particles belonging to this major class were re-extracted unbinned and refined imposing C2 symmetry followed by per particle defocus refinement in RELION-3.0. Further separation to reach high-resolution was achieved by 3D classification using higher T-values (T=8) and subdividing into 6 classes, without alignment. Four of the six classes showed features consistent with Mec1-Ddc2 and were each refined by gold-standard 3D refinement in RELION, with two of the classes reaching ~8 Å (44% class) resolution or worse (21% class) as determined by the FSC=0.143 criterion – suggesting that these were poor quality particles. Two other classes could be refined separately to high-resolution, with particle polishing, 3 rounds of CTF refinement, resulting in reconstructions approaching 3 Å when refined in RELION-3.0 according to the gold-standard refinement procedure and applying C2 symmetry. Auto-refinement of the same particle stacks in cisTEM, using the best reconstruction filtered to 20 Å as a starting model, produces a 2.8 Å reconstruction (FSC = 0.143, which we denote as State I, see main text for details) with features consistent with such estimates (see Extended Data Fig. 6 and Extended Data Fig. 7), and a 3.2 Å reconstruction (FSC = 0.143, which we denote as State II, see main text for details). We also refined the highest resolution particles without symmetry (C1), which converged to 2.9 Å resolution (FSC=0.143) and showed no major overall differences. However, the side chain details in the active site of the C1 map were not as well-defined, which we presume is due to some residual plasticity in active site, as shown by the presence of State I and II in our dataset. The numbers of particles and processing steps are summarized in Extended Data Fig. 5. Local resolution estimates were calculated using ResMap [63] and showed a resolution range of 2.5 Å – 3.7 Å for State I map, and 2.7 Å – 4.3 Å for State II map. Angular distribution plots of both the reconstructions show that this mutant sample does not suffer from severe preferential orientation despite being prepared in an analogous manner to the wild-type sample.

Model Building and Refinement

For map interpretation reconstructions were blurred or sharpened using a range of positive or negative b-factors using MRCtoMTZ in CCPEM [66] to find optimum values of sharpening. The final wild-type maps were sharpened with a b-factor of −40 to −200 Å^2, and the F2244L reconstructions were sharpened using a b-factor of −20 to −60 Å^2. The high-resolution maps permitted accurate model building and therefore the structure was built manually using Coot [67] starting with the C-terminal kinase domain bound to AMP-PNP using the high-resolution nucleotide-bound X-ray structures of mTOR [5,19,20] and EM structures of Mec1 [27], and Tel1 [21] as guides. We also built Ddc2 manually using the Ddc2 chain from the previously determined Mec1-Ddc2 structure (pdb 5X6O) docked into the destiny. We were able to build co-ordinates with the majority of side chains corresponding to Mec1 (UNIPROT accession code P38111) and the majority (residue 189 – C-terminus) of Ddc2 (UNIPROT accession code Q04377). The co-ordinates for the Mec1-Ddc2 dimer model were real space refined in PHENIX [68,69] against the 2.8 Å map (sharpened with a b-factor of −30 Å^2). Refinements were limited to resolutions estimated by CisTEM (at FSC=0.143) to prevent over-fitting. Ramachandran, C_β, non-crystallographic symmetry (NCS), and secondary structure restraints (generated in PHENIX) were imposed throughout the refinement to ensure good model geometry; typically, 3-cycles of real space refinement were run (3 macro cycles of global and local optimization and B-factor refinement), were performed. PHENIX automatically estimates the relative weighting of the restraints and map to prevent overfitting with each cycle and we re-ran real space refinement using the best weighting value. The refined coordinates were validated using MOLPROBITY [70] within PHENIX, and manually adjusted in Coot before re-refinement. The Mec1(F2244L)-Ddc2 model (refined at 2.8 Å) was fitted into the 3.2 Å State II map (sharpened using a b-factor of −30 Å^2) and real space refined in PHENIX using the same procedure as outlined above. The Mec1(F2244L)-Ddc2 model, was fitted into the Mec1-Ddc2:AMP-PNP map at 3.8 Å (sharpened using a b-factor of −60 Å^2) and real space refined in PHENIX using up to 10 macro cycles in the first instance, due to the conformational changes between the two structures. The model was rebuilt in places that differed significantly, such as the activation loop and PRD in the kinase domain. This was subjected to further real space refinements in PHENIX analogous to the mutant structures. Refinement and model statistics are given in Table 1. Map vs model FSC curves were also generated for all structures in PHENIX as part of the refinement procedure and given in Extended Data Fig. 4 and Extended Data Fig. 6).

Model Interpretation and Analysis

Figures were created in PyMOL (Schrodinger, LLC), UCSF Chimera [71] and Chimera X [72]. Structural superpositions were performed in PyMOL. To analyze kinase domain differences, kinase domains were aligned to the catalytic loop. For dimer interface differences, the structures were aligned to a single promoter of Mec1-Ddc2. Interface buried surface area estimates were calculated using PISA [73].

Quantification and Statistical Analysis

CryoEM data were analyzed and quantified using a Bayesian approach as described in RELION [59,74]. No statistical methods were used to predetermine sample size except sufficient images were collected to ensure adequate reconstructions could be obtained.

Reporting Summary

Further information on experimental design is available in the Nature Research Reporting Summary linked to this article.

Data Availability

The cryoEM reconstruction volumes and the atomic co-ordinates generated in this study are available at the EMDB under accession codes, EMD-11050 (nucleotide-bound F2244L mutant State I), EMD-11051 (nucleotide-bound F2244L mutant State II), EMD-11055 (nucleotide-bound wild-type) and EMD-11056 (wild-type), and the RCSB Protein Data Bank under the PDB codes 6Z2W (AMP-PNP-bound F2244L State I), 6Z2X (AMP-PNP-bound F2244L State II), 6Z3A (AMP-PNP-bound wild-type). Source Data for main text figures are provided with this article. Yeast strains, plasmids, and plasmid sequences are available upon request (P.M.B.).

Extended Data

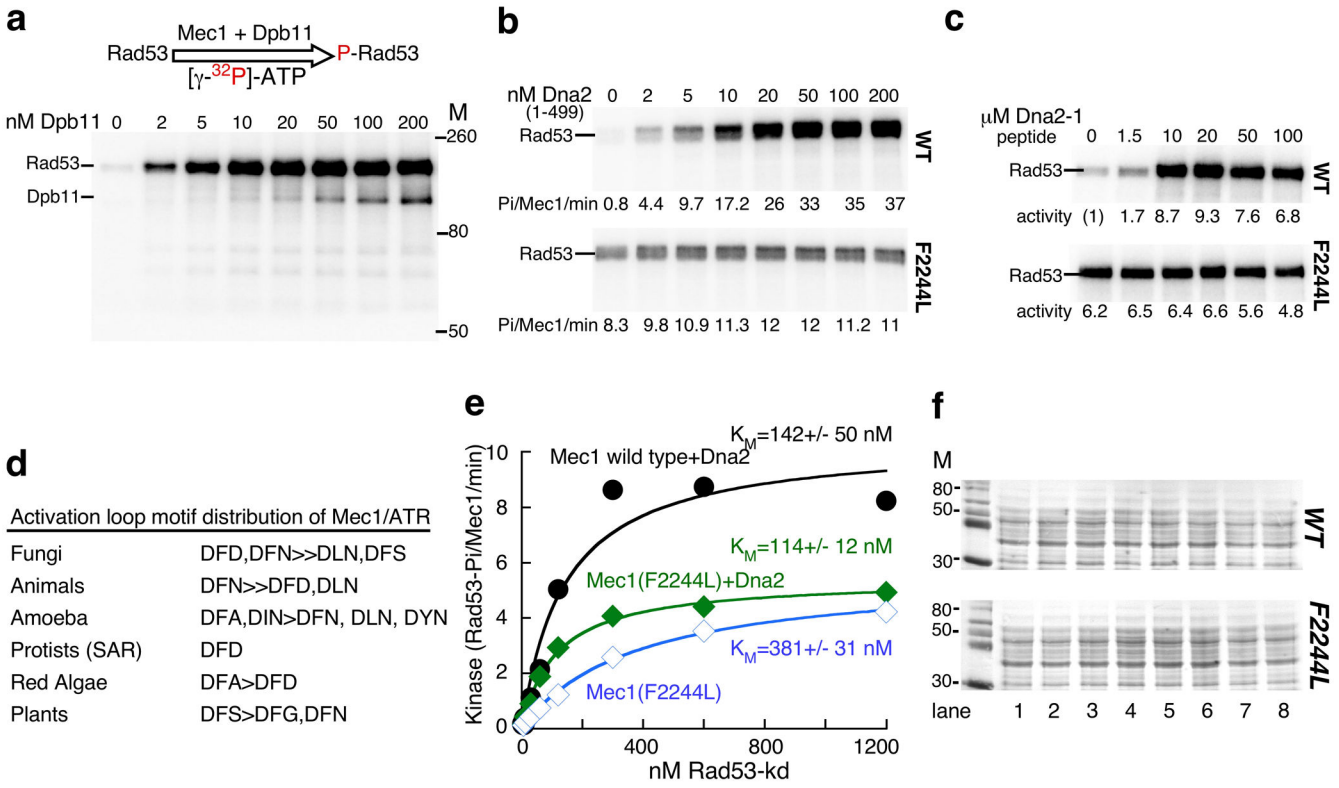

Extended Data Fig. 1. Activation loop mutagenesis of Mec1.

(a) Representative complete gel of Mec1 kinase assay, described in Fig. 2. The gel shown is for the experiment in Fig. 2a, WT.

(b) Kinase activity of Mec1 and Mec1(F2244L) as a function of Dna2(1-499). Phosphorylation rates are given below the gel.

(c) Kinase activity of Mec1 and Mec1(F2244L) as a function of Dna2-1 peptide: HHDFTQDEDGPMEEVIWKYSPLQRDMSDKT. Fold stimulation compared to wild-type Mec1 without activator is given.

(d) Phylogenetic analysis of the activation loop ^{2243}DFD^{2245} motif. 640 eukaryotic Mec1/ATR sequences were aligned with MSAProbs (https://toolkit.tuebingen.mpg.de/), filtered to a set of 95 sequences that showed less than 50% sequence identity, and the motif distribution recorded.

(e) Titration of Rad53 into the Mec1 assay. Standard assays with 3 nM Mec1 and 5 nM Dna2(1-499) activator, or with 3 nM Mec1(F2244L) with or without 5 nM Dna2(1-499) activator were carried out at increasing concentrations of GST-Rad53-kd. Activities are expressed as Rad53 phosphates per Mec1 (monomer) per minute, and the data were modeled to the Michaelis-Menten equation.

(f) Ponceau staining of the extracts used for the Western blots in Fig. 2e.

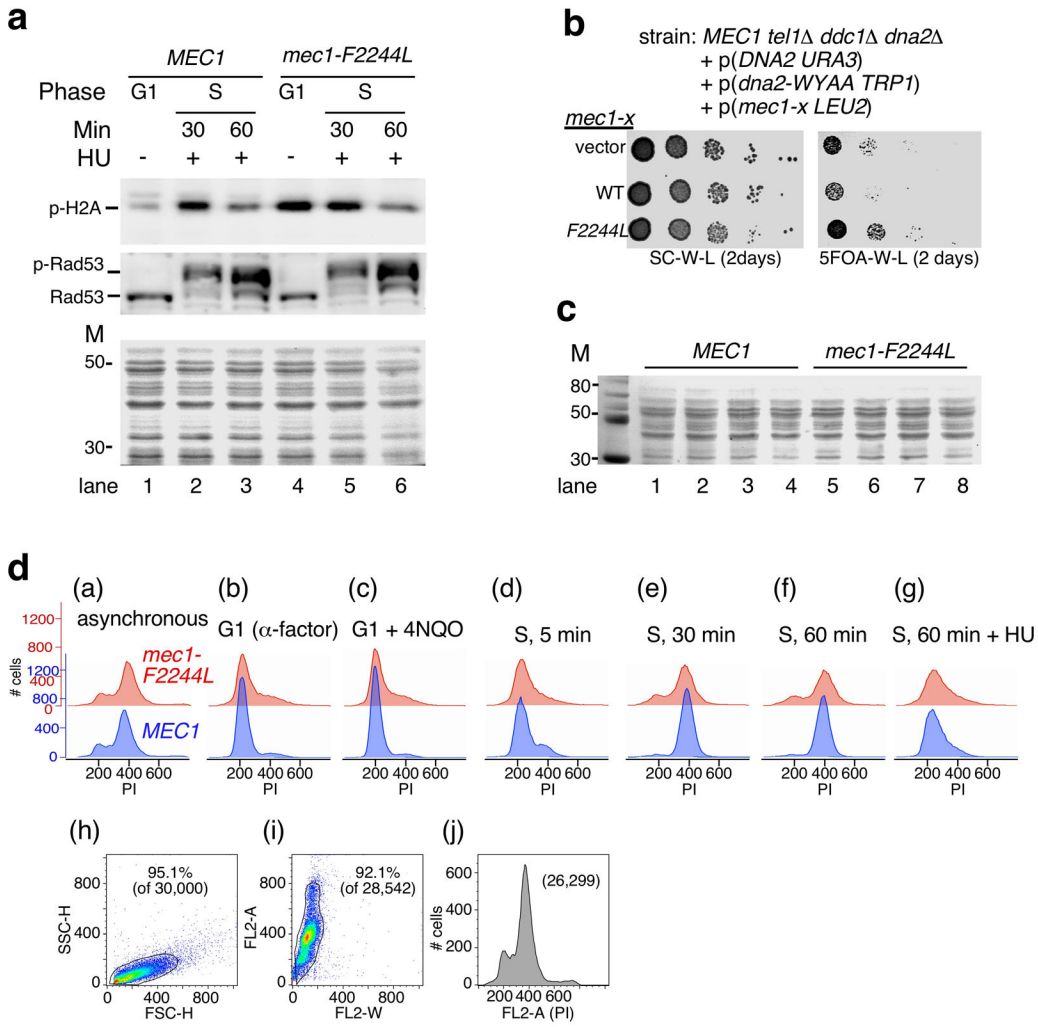

Extended Data Fig. 2. Cell cycle analysis of a *MEC1* mutant with constitutive activity.

(a) Western blot analysis of phospho-H2A (pS129) (top) and Rad53 (bottom) in wild-type strain PY405, with either *MEC1* or *mec1-F2244L*. Cells were arrested in G1 phase with alpha-factor, or arrested in G1 phase with alpha-factor, and released into S phase with 200 mM of hydroxyurea for the indicated time. Ponceau staining of the blot is shown below.

(b) *mec1-F2244L* suppresses the growth defect of activator-defective yeast. In the experimental scheme, the extreme defects of the activator-defective strain were initially suppressed by a plasmid-borne copy of wild-type *DNA2*, containing the *URA3* gene as selectable and counterselectable marker. Thus, strain *MEC1 tel1Δ ddc1Δ dna2Δ* (PY270) contains three plasmids: p(*DNA2 URA3*), p(*dna2-WYAA TRP1*), and either vector or p(*mec1-x LEU2*). The strains were grown on media lacking Trp and Leu (left), or on 5FOA-containing media (right) that only permits growth if the p(*DNA2 URA3*) plasmid is lost. The data indicate that *mec1-F2244L* allows cell growth without p(*DNA2 URA3*), therefore suppressing the growth defect of the activator-defective strain.

(c) Ponceau staining of the extracts used for the blots in Fig. 2g.

(d) Constitutively active *mec1-F2244L* progresses slowly through S phase. Strain PY406 containing p(*MEC1 LEU2*) (blue) or p(*mec1-F2244L LEU2*) (red). Cell cycle distribution

was measured for (a) asynchronous cells; (b) alpha-factor arrested G1 cells; (c) G1 arrested cells treated with 4NQO for 30 min; (d, e, f) G1 arrested cells released into fresh YPD for 5, 30, and 60 minutes; (g) G1 arrested cells released into fresh YPD containing 200 mM hydroxyurea for 60 minutes, (h, i, j) example of gating strategy shown for plot (a) p(*MEC1 LEU2*) asynchronous cells.

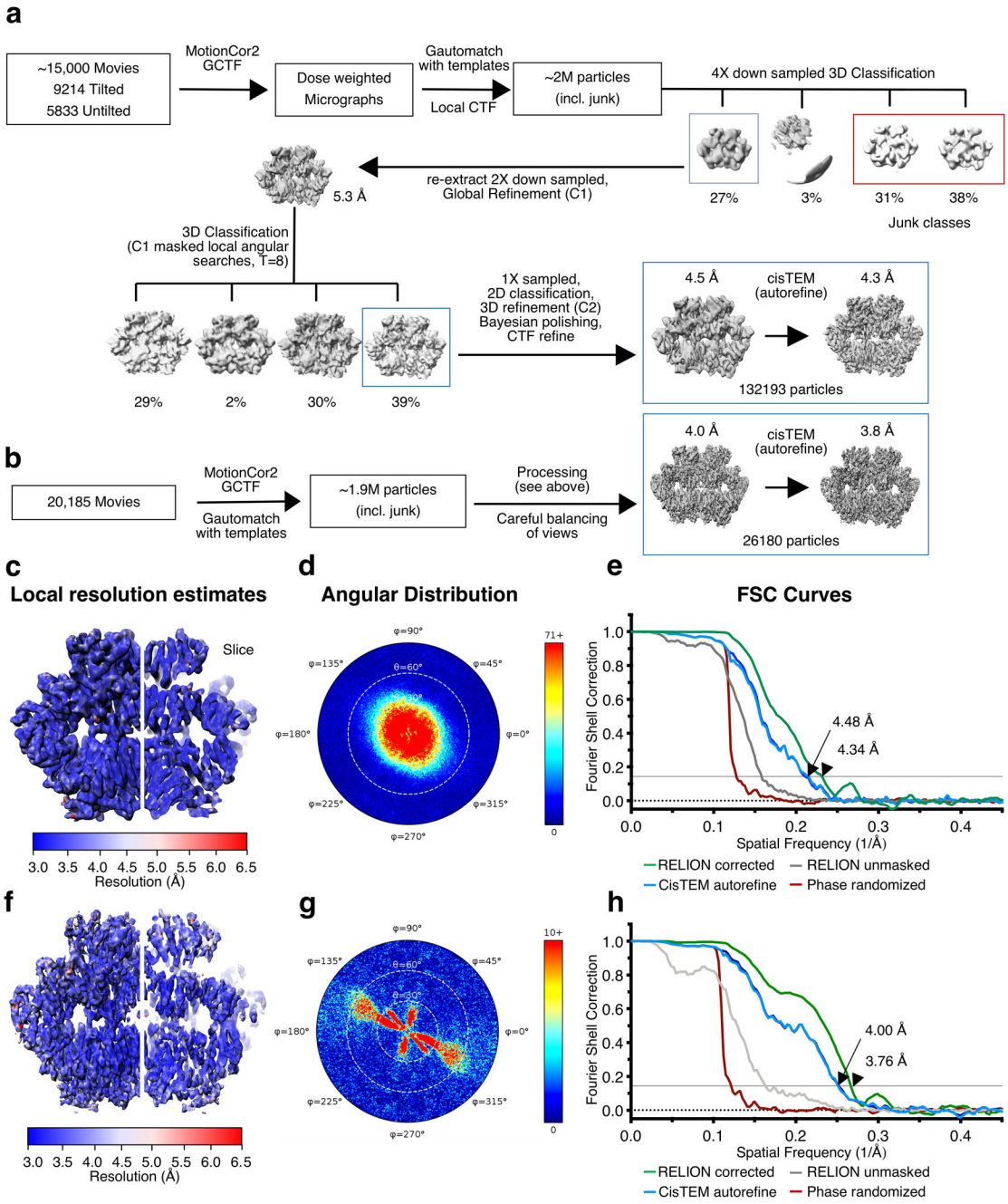

Extended Data Fig. 3. CryoEM processing and reconstruction quality of Mec1-Ddc2.
(a, b) Processing tree resulting reconstructions of Mec1-Ddc2 and a second reconstruction in complex with AMP-PNP (see methods for details). **(c, f)** Local resolution estimates from

ResMap, with slice through the density to show internal features, of apo **(c)** and bound with AMP-PNP **(f)**.

(d, g) Angular distribution from CisTEM autorefine, and **(e, h)** Gold-standard Fourier shell correlation (FSC) from RELION-3.0 and CisTEM.

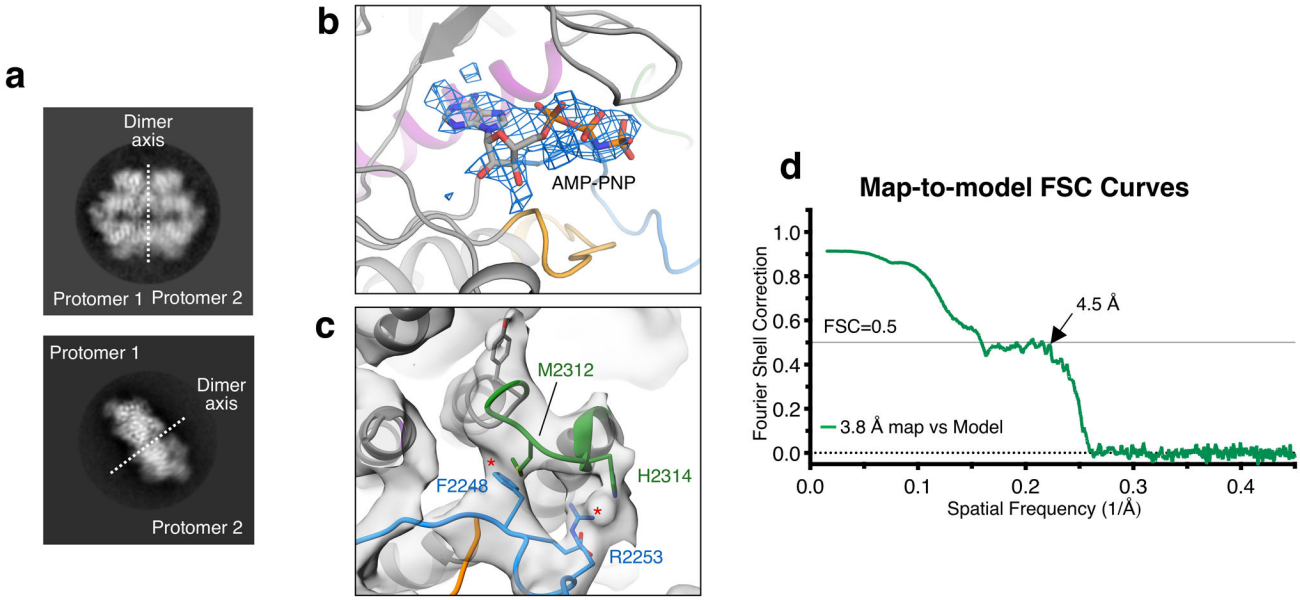

Extended Data Fig. 4. Map and model features of the Mec1-Ddc2 complex.

(a) 2D classes of Mec1-Ddc2 after a focused 3D refinement masking on Mec1-Ddc2 heterodimer, showing intrinsic flexibility of the complex across the dimer interface.

(b) Electron density features of the bound AMP-PNP, and **(c)** strong electron density (unsharpened map) showing the PRD-I interaction with the activation loop at two points (asterisked).

(d) Map to model FSC curves.

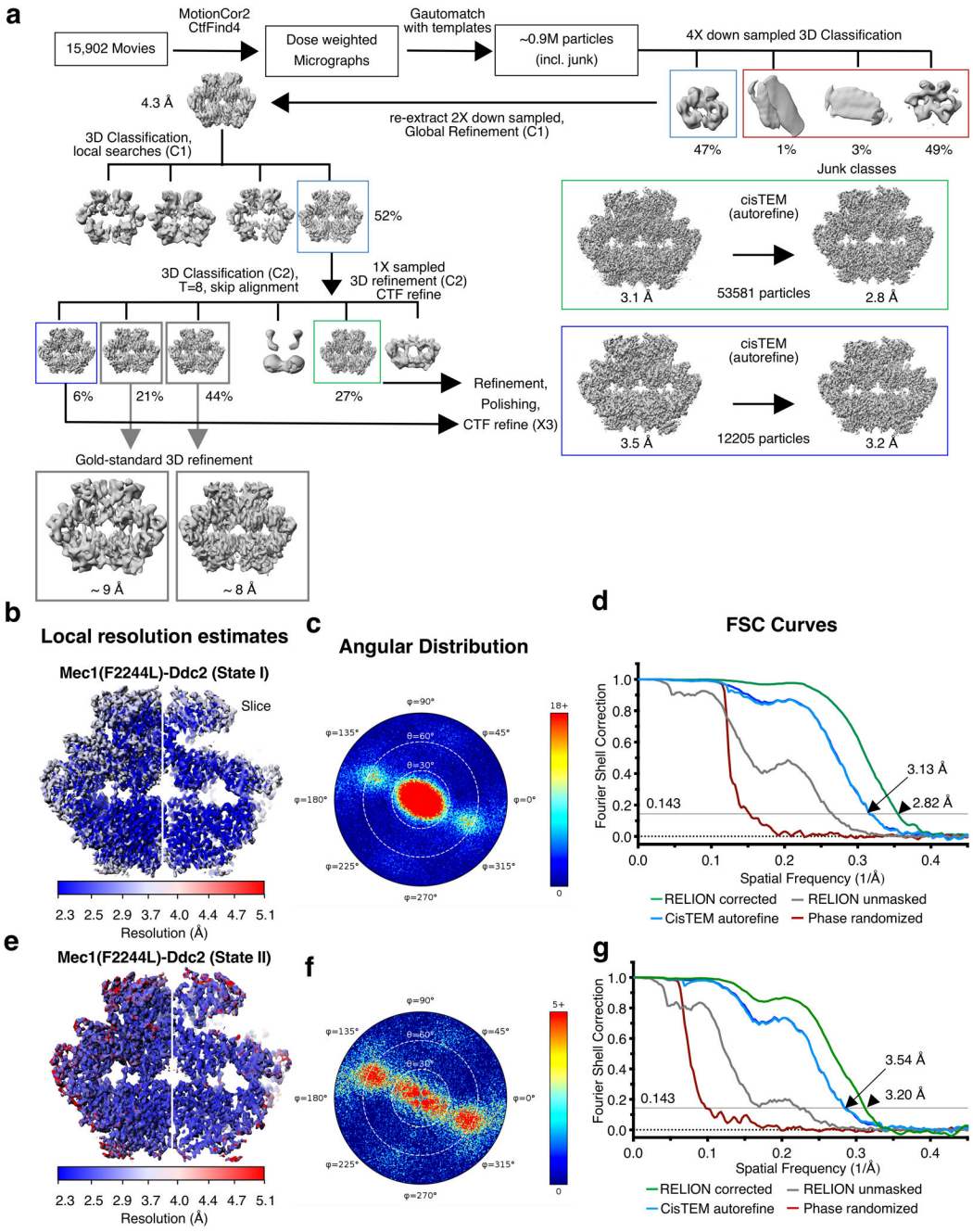

Extended Data Fig. 5. CryoEM processing and reconstruction quality of Mec1(F2244L)-Ddc2.

(a) Processing tree resulting in high resolution reconstructions of Mec1(F2244L)-Ddc2 in complex with AMP-PNP and magnesium captured in two states (see Methods). **(b)** Local resolution estimates from ResMap, with slice through the density to show internal features, of State I, **(c)** angular distribution from CisTEM autorefine, and **(d)** Gold-standard Fourier shell correlation (FSC) from RELION-3.0 and CisTEM.

(e) Local resolution estimates from ResMap of State II, with **(f)** angular distribution from CisTEM autorefine, and **(g)** Gold-standard Fourier shell correlation (FSC) from RELION-3.0 and CisTEM.

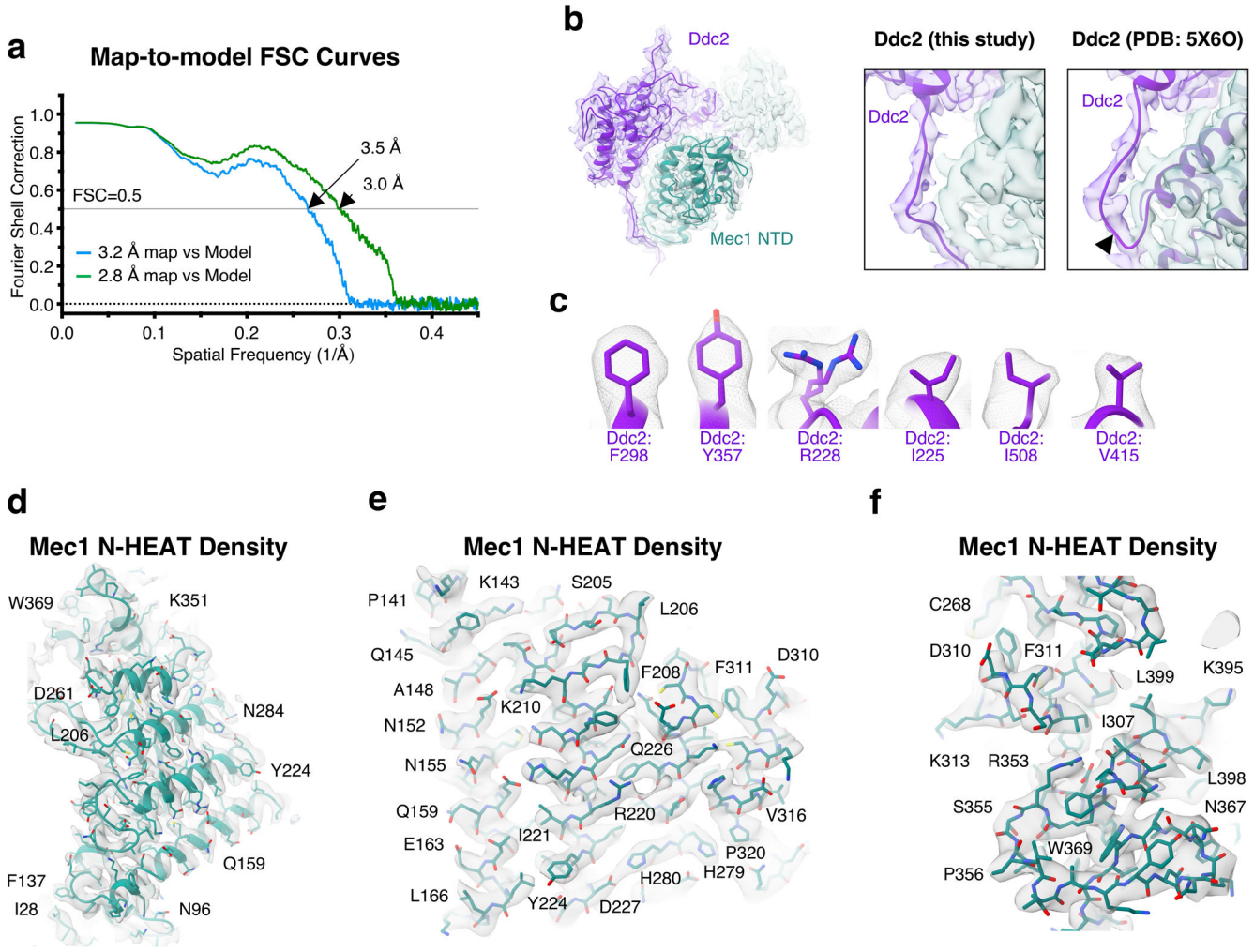

Extended Data Fig. 6. Data and model quality of the Mec1(F2244L)-Ddc2 reconstruction.

(a) Map to model FSC curves of the F2244 mutant reconstruction.

(b) Ddc2 and Mec1 N-terminal domain density (NTD) and model showing clear separation of Mec1 and Ddc2 proteins for accurate model building of this region (*left*), with close-up views of chain tracing between the model built in this study (*middle*) and the previously published model (PDB:5X6O) (*right*). The arrow indicates the point at which the two models diverge.

(c) High-resolution features from the 2.8 Å map, showing that the electron density quality is sufficient to resolve types of aromatic residues (Phenylalanine over Tyrosines), β–branched side chains (Isoleucine), as well as smaller hydrophobics (Valine) and an example of a split conformation of Arginine.

(d-f) CryoEM density regions of the Mec1 N-terminal domain (~300 amino acids) showing the overall fit of the model and side chains (labeled), along with close-up views of different regions showing unambiguous side chain density for accurate model building.

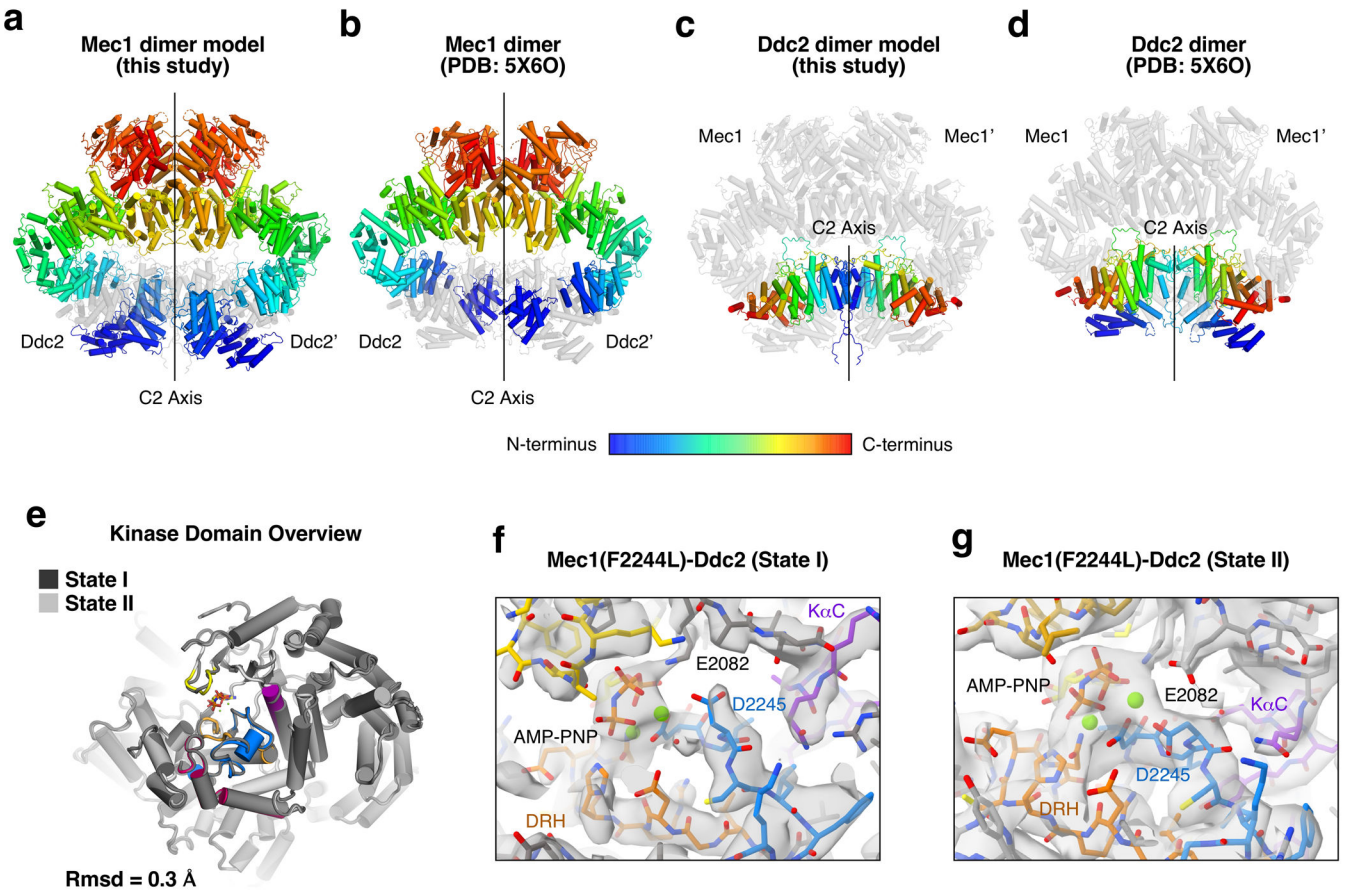

Extended Data Fig. 7. Global and kinase domain structural comparisons of Mec1-Ddc2.

(a-d) Structural comparisons between the Mec1 model **(a,b)** and Ddc2 model **(c,d)** from this study and the PDB:5X6O showing the global differences in N-terminal domains of both proteins.

(e-g) Overall comparison between the kinase region of Mec1(F2244L) State I (grey) and State II (light grey), demonstrating that both states are very similar outside of the active site with an Rmsd = 0.3 Å.

(f-g) Electron density of the nucleotide binding site and different side chain conformations associated with State I and State II (see main text for details).

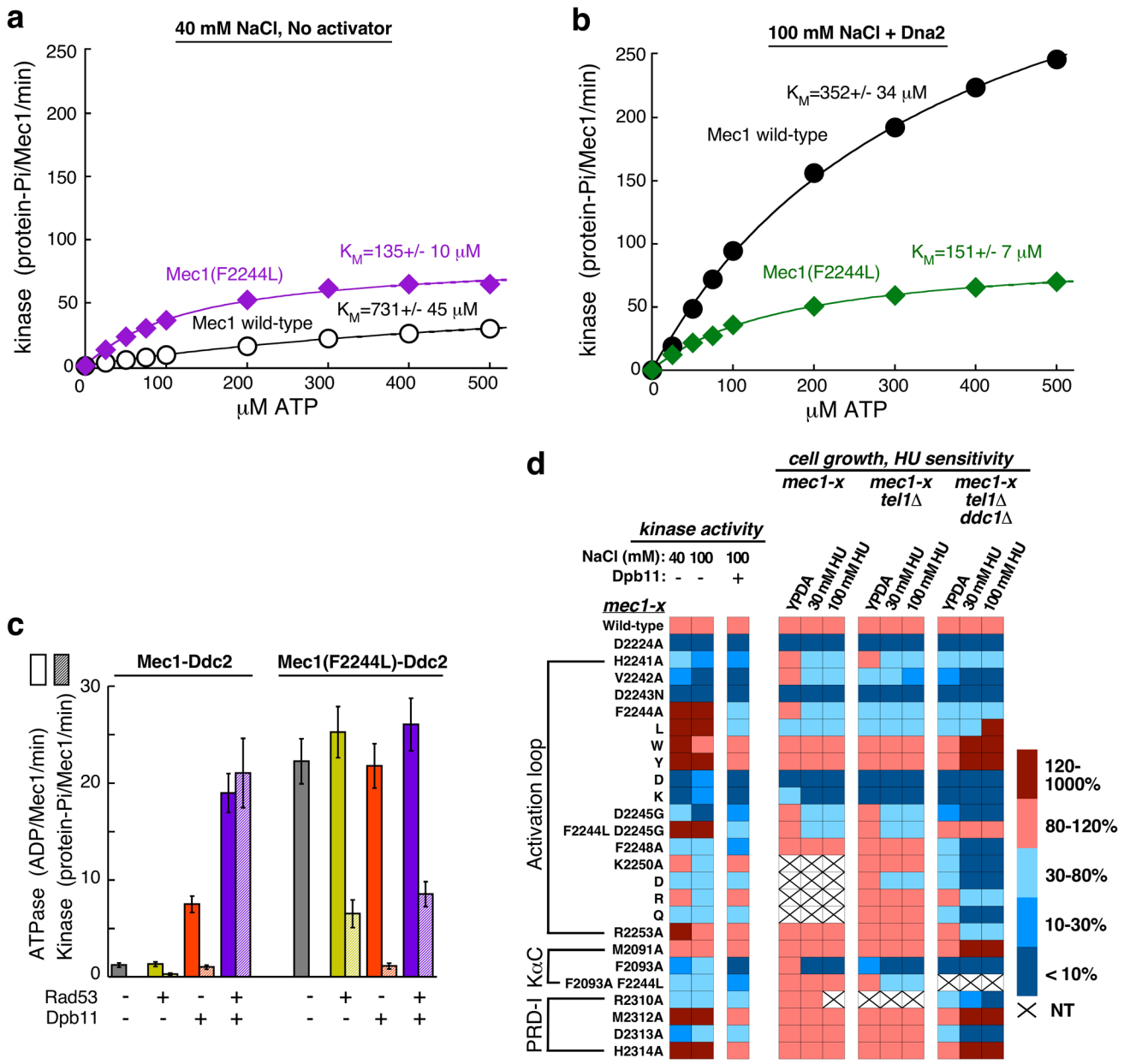

Extended Data Fig. 8. ATP dependence of Mec1 activity.

(**a**) Standard Mec1 kinase assays without activator at 40 mM NaCl, or **(b)** with 200 nM Dna2(1-499) at 100 mM NaCl, were carried out at increasing concentrations of ATP. Activities are expressed as protein phosphates (Rad53 plus Dna2(1-499) when relevant) per Mec1 (monomer) per minute.

(c) Comparative ATPase (solid bars) and kinase (striped bars) activities of Mec1-Ddc2 and Mec1(F2244L)-Ddc2, in the presence or absence of Rad53 and Dpb11 (see Methods).

(d) Summary of phenotypes of all Mec1 mutants. The *in vitro* and *in vivo* phenotypes of the mutants are shown in the form of heat maps using Prism 8 GraphPad software.

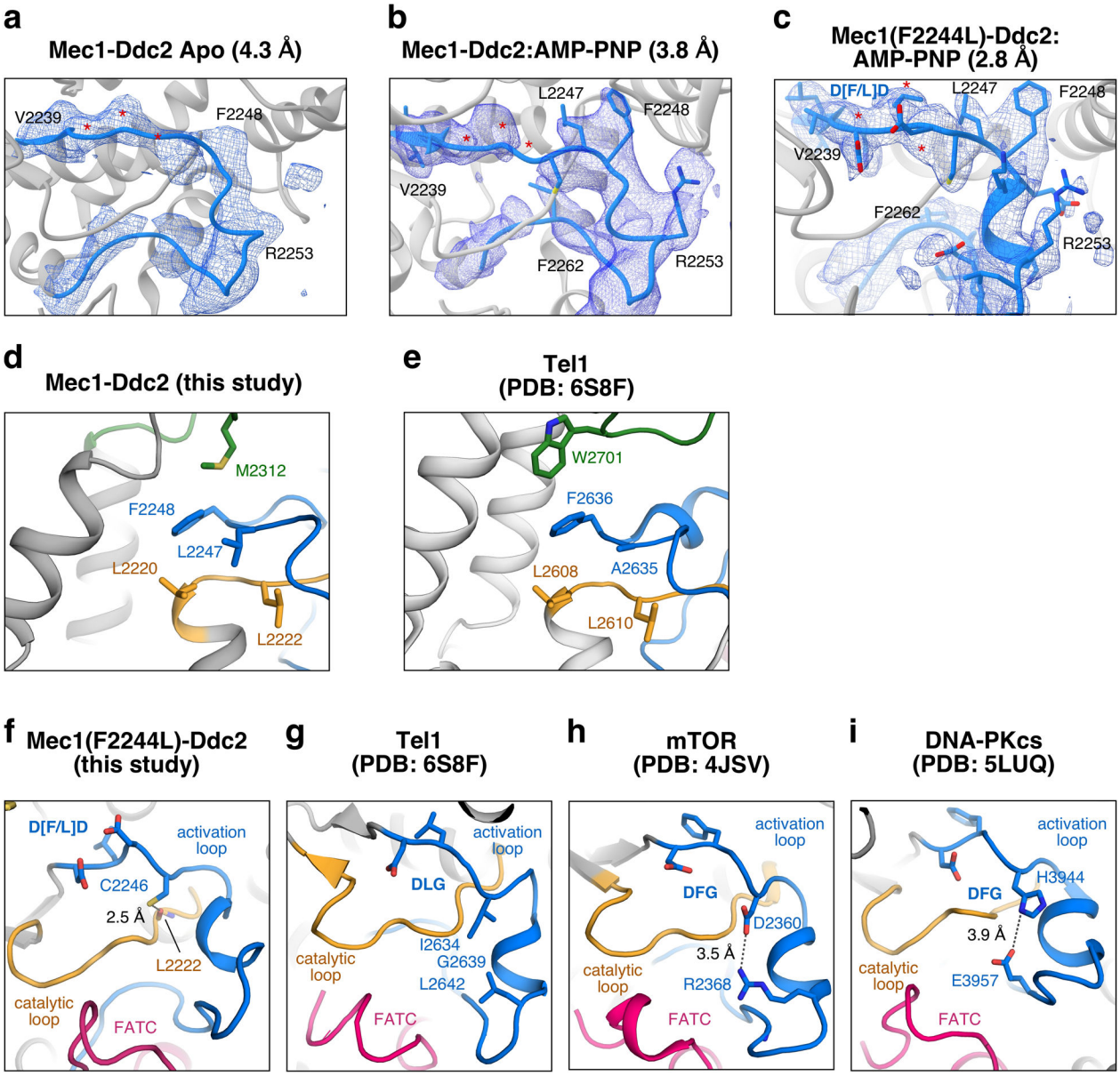

Extended Data Fig. 9. Structural analysis and comparisons of Mec1.

(a-c) Electron density of the activation loop from the apo **(a)**, AMP-PNP-bound **(b)** and AMP-PNP-bound F2244L mutant **(c)**, showing that in all cases the activation loop remains ordered, with flexibility around the DFD-motif (asterisks), which could not be easily resolved in the wild-type structures. Several large residues are shown as landmarks.

(d,e) PRD-I hydrophobic network comparisons between Mec1-Ddc2 **(e)** and Tel1 **(e)**, suggesting that M2312 plays an analogous role to W2701 in Tel1. PRD-I, activation loop and catalytic loop are colored as in Fig. 1b.

(f-i) Comparison of stabilizing interactions in activations loops across PIKKs. **(f)** In Mec1, the DFD+1 residue plays a role in stabilizing the activation loop. In our activated structure the thiol group of the invariant C2246 forms an H-bond with the main chain carbonyl of L2222 of the catalytic loop, helping to stabilize the active state. In Tel1 the DLG+1 (I2634)

forms a hydrophobic spline with G2639 and L2642 of the activation loop **(g)**, whereas in mTOR **(h)** and DNA-PKcs **(i)** an ion pair is preferred.

Supplementary Material

Refer to Web version on PubMed Central for supplementary material.

Acknowledgements

We thank Burgers lab members Carrie Stith and Bonnie Yoder for strains construction, and James Haber (Brandeis University) for plasmids. We thank Andrea Nan (Francis Crick Institute), Katie Cunnea (eBIC) and Yun Song (eBIC) for their support with cryoEM data acquisition, and Zhang lab members Rafa Ayala for help with initial screening and Rhys Williams for useful discussions. Initial cryoEM screening of samples was carried out at Imperial College London Center for Structural Biology EM facility. High-resolution cryoEM data were collected at the eBIC (proposal EM19865). eBIC is funded by the Wellcome Trust, MRC, and BBSRC. This work was funded in part by grant GM118129 from the National Institutes of Health (to P.M.B.) and the Wellcome Trust 210658/Z/18/Z (to X.Z.).

References

1. Weber AM & Ryan AJ ATM and ATR as therapeutic targets in cancer. Pharmacol Ther 149, 124–38 (2015). [PubMed: 25512053]
2. Lovejoy CA & Cortez D Common mechanisms of PIKK regulation. DNA Repair (Amst) 8, 1004–8 (2009). [PubMed: 19464237]
3. Kumagai A, Lee J, Yoo HY & Dunphy WG TopBP1 activates the ATR-ATRIP complex. Cell 124, 943–55 (2006). [PubMed: 16530042]
4. Mordes DA, Nam EA & Cortez D Dpb11 activates the Mec1-Ddc2 complex. Proc Natl Acad Sci U S A 105, 18730–4 (2008). [PubMed: 19028869]
5. Mordes DA, Glick GG, Zhao R & Cortez D TopBP1 activates ATR through ATRIP and a PIKK regulatory domain. Genes Dev 22, 1478–89 (2008). [PubMed: 18519640]
6. Navadgi-Patil VM & Burgers PM Yeast DNA replication protein Dpb11 activates the Mec1/ATR checkpoint kinase. J Biol Chem 283, 35853–9 (2008). [PubMed: 18922789]
7. Navadgi-Patil VM & Burgers PM The unstructured C-terminal tail of the 9-1-1 clamp subunit Ddc1 activates Mec1/ATR via two distinct mechanisms. Mol Cell 36, 743–53 (2009). [PubMed: 20005839]
8. Kumar S & Burgers PM Lagging strand maturation factor Dna2 is a component of the replication checkpoint initiation machinery. Genes Dev 27, 313–21 (2013). [PubMed: 23355394]
9. Paull TT Mechanisms of ATM Activation. Annu Rev Biochem 84, 711–38 (2015). [PubMed: 25580527]
10. Hailemariam S, Kumar S & Burgers PM Activation of Tel1(ATM) kinase requires Rad50 ATPase and long nucleosome-free DNA but no DNA ends. J Biol Chem 294, 10120–10130 (2019). [PubMed: 31073030]
11. Wanrooij PH, Tannous E, Kumar S, Navadgi-Patil VM & Burgers PM Probing the Mec1ATR Checkpoint Activation Mechanism with Small Peptides. J Biol Chem 291, 393–401 (2016). [PubMed: 26499799]
12. Thada V & Cortez D Common motifs in ETAA1 and TOPBP1 required for ATR kinase activation. J Biol Chem 294, 8395–8402 (2019). [PubMed: 30940728]
13. Sawicka M et al. The Dimeric Architecture of Checkpoint Kinases Mec1ATR and Tel1ATM Reveal a Common Structural Organization. J Biol Chem 291, 13436–47 (2016). [PubMed: 27129217]
14. Ball HL & Cortez D ATRIP oligomerization is required for ATR-dependent checkpoint signaling. J Biol Chem 280, 31390–6 (2005). [PubMed: 16027118]
15. Deshpande I et al. Structural Basis of Mec1-Ddc2-RPA Assembly and Activation on Single-Stranded DNA at Sites of Damage. Mol Cell 68, 431–445 e5 (2017). [PubMed: 29033322]

16. Zou L & Elledge SJ Sensing DNA damage through ATRIP recognition of RPA-ssDNA complexes. [see comment]. Science. 300, 1542–8 (2003). [PubMed: 12791985]
17. Memisoglu G et al. Mec1(ATR) Autophosphorylation and Ddc2(ATRIP) Phosphorylation Regulates DNA Damage Checkpoint Signaling. Cell Rep 28, 1090–1102.e3 (2019). [PubMed: 31340146]
18. Adams JA Kinetic and catalytic mechanisms of protein kinases. Chem Rev 101, 2271–90 (2001). [PubMed: 11749373]
19. Lempiainen H & Halazonetis TD Emerging common themes in regulation of PIKKs and PI3Ks. EMBO J 28, 3067–73 (2009). [PubMed: 19779456]
20. Yang H et al. mTOR kinase structure, mechanism and regulation. Nature 497, 217–23 (2013). [PubMed: 23636326]
21. Yates LA et al. Cryo-EM Structure of Nucleotide-Bound Tel1(ATM) Unravels the Molecular Basis of Inhibition and Structural Rationale for Disease-Associated Mutations. Structure 28, 96–104 e3 (2020). [PubMed: 31740029]
22. Sibanda BL, Chirgadze DY, Ascher DB & Blundell TL DNA-PKcs structure suggests an allosteric mechanism modulating DNA double-strand break repair. Science 355, 520–524 (2017). [PubMed: 28154079]
23. Gat Y et al. InsP6 binding to PIKK kinases revealed by the cryo-EM structure of an SMG1-SMG8-SMG9 complex. Nat Struct Mol Biol 26, 1089–1093 (2019). [PubMed: 31792449]
24. Jansma M et al. Near-Complete Structure and Model of Tel1ATM from Chaetomium thermophilum Reveals a Robust Autoinhibited ATP State. Structure 28, 83–95 e5 (2020). [PubMed: 31740028]
25. Mallory JC & Petes TD Protein kinase activity of Tel1p and Mec1p, two Saccharomyces cerevisiae proteins related to the human ATM protein kinase. Proc Natl Acad Sci U S A 97, 13749–54 (2000). [PubMed: 11095737]
26. Paciotti V, Clerici M, Scotti M, Lucchini G & Longhese MP Characterization of mec1 kinase-deficient mutants and of new hypomorphic mec1 alleles impairing subsets of the DNA damage response pathway. Mol Cell Biol 21, 3913–25 (2001). [PubMed: 11359899]
27. Wang X et al. 3.9 Å structure of the yeast Mec1-Ddc2 complex, a homolog of human ATR-ATRIP. Science 358, 1206–1209 (2017). [PubMed: 29191911]
28. Rao Q et al. Cryo-EM structure of human ATR-ATRIP complex. Cell Res 28, 143–156 (2018). [PubMed: 29271416]
29. Ball HL et al. Function of a conserved checkpoint recruitment domain in ATRIP proteins. Mol Cell Biol 27, 3367–77 (2007). [PubMed: 17339343]
30. Gangadhara G et al. A class of highly selective inhibitors bind to an active state of PI3Kgamma. Nat Chem Biol 15, 348–357 (2019). [PubMed: 30718815]
31. Wanrooij PH & Burgers PM Yet another job for Dna2: Checkpoint activation. DNA Repair (Amst) 32, 17–23 (2015). [PubMed: 25956863]
32. Jacobsen DM, Bao ZQ, O'Brien P, Brooks CL 3rd & Young MA Price to be paid for two-metal catalysis: magnesium ions that accelerate chemistry unavoidably limit product release from a protein kinase. J Am Chem Soc 134, 15357–70 (2012). [PubMed: 22891849]
33. Burtelow MA, Roos-Mattjus PM, Rauen M, Babendure JR & Karnitz LM Reconstitution and molecular analysis of the hRad9-hHus1-hRad1 (9–1-1) DNA damage responsive checkpoint complex. J Biol Chem. 276, 25903–9 (2001). [PubMed: 11340080]
34. Majka J & Burgers PM Yeast Rad17/Mec3/Ddc1: a sliding clamp for the DNA damage checkpoint. Proc. Natl. Acad. Sci. USA 100, 2249–2254 (2003). [PubMed: 12604797]
35. Allen JB, Zhou Z, Siede W, Friedberg EC & Elledge SJ The SAD1/RAD53 protein kinase controls multiple checkpoints and DNA damage-induced transcription in yeast. Genes Dev. 8, 2401–2415 (1994). [PubMed: 7958905]
36. Sanchez Y et al. Regulation of RAD53 by the ATM-like kinases MEC1 and TEL1 in yeast cell cycle checkpoint pathways. Science 271, 357–60 (1996). [PubMed: 8553072]
37. Ma JL, Lee SJ, Duong JK & Stern DF Activation of the checkpoint kinase Rad53 by the phosphatidyl inositol kinase-like kinase Mec1. J Biol Chem 281, 3954–63 (2006). [PubMed: 16365046]

38. Downs JA, Lowndes NF & Jackson SP A role for Saccharomyces cerevisiae histone H2A in DNA repair. Nature 408, 1001–4 (2000). [PubMed: 11140636]
39. Fink M, Imholz D & Thoma F Contribution of the serine 129 of histone H2A to chromatin structure. Mol Cell Biol 27, 3589–600 (2007). [PubMed: 17353265]
40. Puddu F, Piergiovanni G, Plevani P & Muzi-Falconi M Sensing of replication stress and Mec1 activation act through two independent pathways involving the 9–1-1 complex and DNA polymerase epsilon. PLoS Genet 7, e1002022 (2011). [PubMed: 21436894]
41. Lanz MC et al. Separable roles for Mec1/ATR in genome maintenance, DNA replication, and checkpoint signaling. Genes Dev 32, 822–835 (2018). [PubMed: 29899143]
42. Bandhu A, Kang J, Fukunaga K, Goto G & Sugimoto K Ddc2 mediates Mec1 activation through a Ddc1- or Dpb11-independent mechanism. PLoS Genet 10, e1004136 (2014). [PubMed: 24586187]
43. Rouse J & Jackson SP Lcd1p recruits Mec1p to DNA lesions in vitro and in vivo. Molecular Cell. 9, 857–869 (2002). [PubMed: 11983176]
44. Huse M & Kuriyan J The conformational plasticity of protein kinases. Cell 109, 275–82 (2002). [PubMed: 12015977]
45. Bao ZQ, Jacobsen DM & Young MA Briefly bound to activate: transient binding of a second catalytic magnesium activates the structure and dynamics of CDK2 kinase for catalysis. Structure 19, 675–90 (2011). [PubMed: 21565702]
46. Williams RM, Yates LA & Zhang X Structures and regulations of ATM and ATR, master kinases in genome integrity. Curr Opin Struct Biol 61, 98–105 (2020). [PubMed: 31924595]
47. Ung PM & Schlessinger A DFGmodel: predicting protein kinase structures in inactive states for structure-based discovery of type-II inhibitors. ACS Chem Biol 10, 269–78 (2015). [PubMed: 25420233]
48. Modi V & Dunbrack RL Jr. Defining a new nomenclature for the structures of active and inactive kinases. Proc Natl Acad Sci U S A 116, 6818–6827 (2019). [PubMed: 30867294]
49. Jauch R et al. Mitogen-activated protein kinases interacting kinases are autoinhibited by a reprogrammed activation segment. EMBO J 25, 4020–32 (2006). [PubMed: 16917500]
50. Yang H et al. Mechanisms of mTORC1 activation by RHEB and inhibition by PRAS40. Nature 552, 368–373 (2017). [PubMed: 29236692]
51. Yin X, Liu M, Tian Y, Wang J & Xu Y Cryo-EM structure of human DNA-PK holoenzyme. Cell Res 27, 1341–1350 (2017). [PubMed: 28840859]
52. Bastidas AC et al. Phosphoryl transfer by protein kinase A is captured in a crystal lattice. J Am Chem Soc 135, 4788–98 (2013). [PubMed: 23458248]

Methods-only references

53. McDonald JP, Levine AS & Woodgate R The Saccharomyces cerevisiae RAD30 gene, a homologue of Escherichia coli dinB and umuC, is DNA damage inducible and functions in a novel error-free postreplication repair mechanism. Genetics 147, 1557–68 (1997). [PubMed: 9409821]
54. Zhao X, Muller EG & Rothstein R A suppressor of two essential checkpoint genes identifies a novel protein that negatively affects dNTP pools. Mol Cell 2, 329–40 (1998). [PubMed: 9774971]
55. Chabes A, Domkin V & Thelander L Yeast Sml1, a protein inhibitor of ribonucleotide reductase. J Biol Chem 274, 36679–83 (1999). [PubMed: 10593972]
56. Hailemariam S et al. The telomere-binding protein Rif2 and ATP-bound Rad50 have opposing roles in the activation of yeast Tel1(ATM) kinase. J Biol Chem 294, 18846–18852 (2019). [PubMed: 31640985]
57. Hustedt N & Shimada K Analyzing DNA replication checkpoint in budding yeast. Methods Mol Biol 1170, 321–41 (2014). [PubMed: 24906321]
58. Zheng SQ et al. MotionCor2: anisotropic correction of beam-induced motion for improved cryo-electron microscopy. Nat Methods 14, 331–332 (2017). [PubMed: 28250466]
59. Zivanov J et al. New tools for automated high-resolution cryo-EM structure determination in RELION-3. Elife 7(2018).

60. Zhang K Gctf: Real-time CTF determination and correction. J Struct Biol 193, 1–12 (2016). [PubMed: 26592709]
61. Zivanov J, Nakane T & Scheres SHW A Bayesian approach to beam-induced motion correction in cryo-EM single-particle analysis. IUCrJ 6, 5–17 (2019).
62. Grant T, Rohou A & Grigorieff N cisTEM, user-friendly software for single-particle image processing. Elife 7(2018).
63. Kucukelbir A, Sigworth FJ & Tagare HD Quantifying the local resolution of cryo-EM density maps. Nat Methods 11, 63–5 (2014). [PubMed: 24213166]
64. Tan YZ et al. Addressing preferred specimen orientation in single-particle cryo-EM through tilting. Nat Methods 14, 793–796 (2017). [PubMed: 28671674]
65. Rohou A & Grigorieff N CTFFIND4: Fast and accurate defocus estimation from electron micrographs. J Struct Biol 192, 216–21 (2015). [PubMed: 26278980]
66. Burnley T, Palmer CM & Winn M Recent developments in the CCP-EM software suite. Acta Crystallogr D Struct Biol 73, 469–477 (2017). [PubMed: 28580908]
67. Emsley P & Cowtan K Coot: model-building tools for molecular graphics. Acta Crystallogr D Biol Crystallogr 60, 2126–32 (2004). [PubMed: 15572765]
68. Afonine PV et al. New tools for the analysis and validation of cryo-EM maps and atomic models. Acta Crystallogr D Struct Biol 74, 814–840 (2018). [PubMed: 30198894]
69. Adams PD et al. PHENIX: a comprehensive Python-based system for macromolecular structure solution. Acta Crystallogr D Biol Crystallogr 66, 213–21 (2010). [PubMed: 20124702]
70. Chen VB, Wedell JR, Wenger RK, Ulrich EL & Markley JL MolProbity for the masses-of data. J Biomol NMR 63, 77–83 (2015). [PubMed: 26195077]
71. Pettersen EF et al. UCSF Chimera--a visualization system for exploratory research and analysis. J Comput Chem 25, 1605–12 (2004). [PubMed: 15264254]
72. Goddard TD et al. UCSF ChimeraX: Meeting modern challenges in visualization and analysis. Protein Sci 27, 14–25 (2018). [PubMed: 28710774]
73. Krissinel E & Henrick K Inference of macromolecular assemblies from crystalline state. J Mol Biol 372, 774–97 (2007). [PubMed: 17681537]
74. Scheres SH RELION: implementation of a Bayesian approach to cryo-EM structure determination. J Struct Biol 180, 519–30 (2012). [PubMed: 23000701]

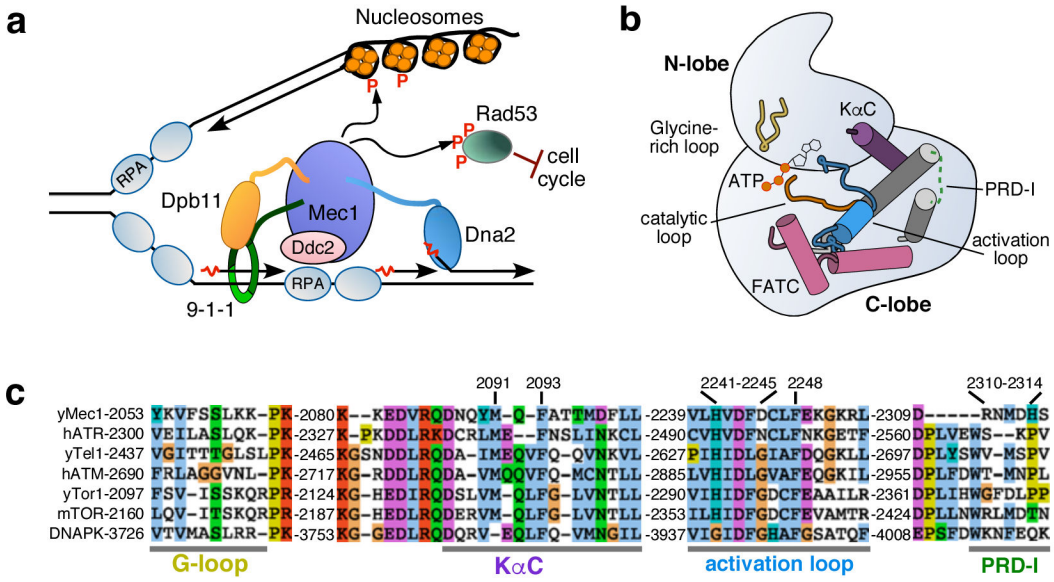

Figure 1: Model of Mec1^{ATR} function and PIKK activation

(a) Simplified model of the yeast DNA replication fork and replication stress response through Mec1-Ddc2 and its activators. The yeast activators shown are the Ddc1^{Rad9} subunit of the 9-1-1 checkpoint clamp, the replication initiator protein Dbp11^{TopBP1}, and the nuclease-helicase Dna2. These three proteins have unstructured CTDs (Ddc1, Dpb11) or NTD (Dna2), which mediate activation.

(b) Structural model of relevant helices and loops of the Mec1 kinase domain.

(c) Sequence alignment of yeast Mec1 and human ATR with other members of the PIKK class, representing the regions and specific residues targeted in this study. The PRD-I residues were realigned based on structural conservation.

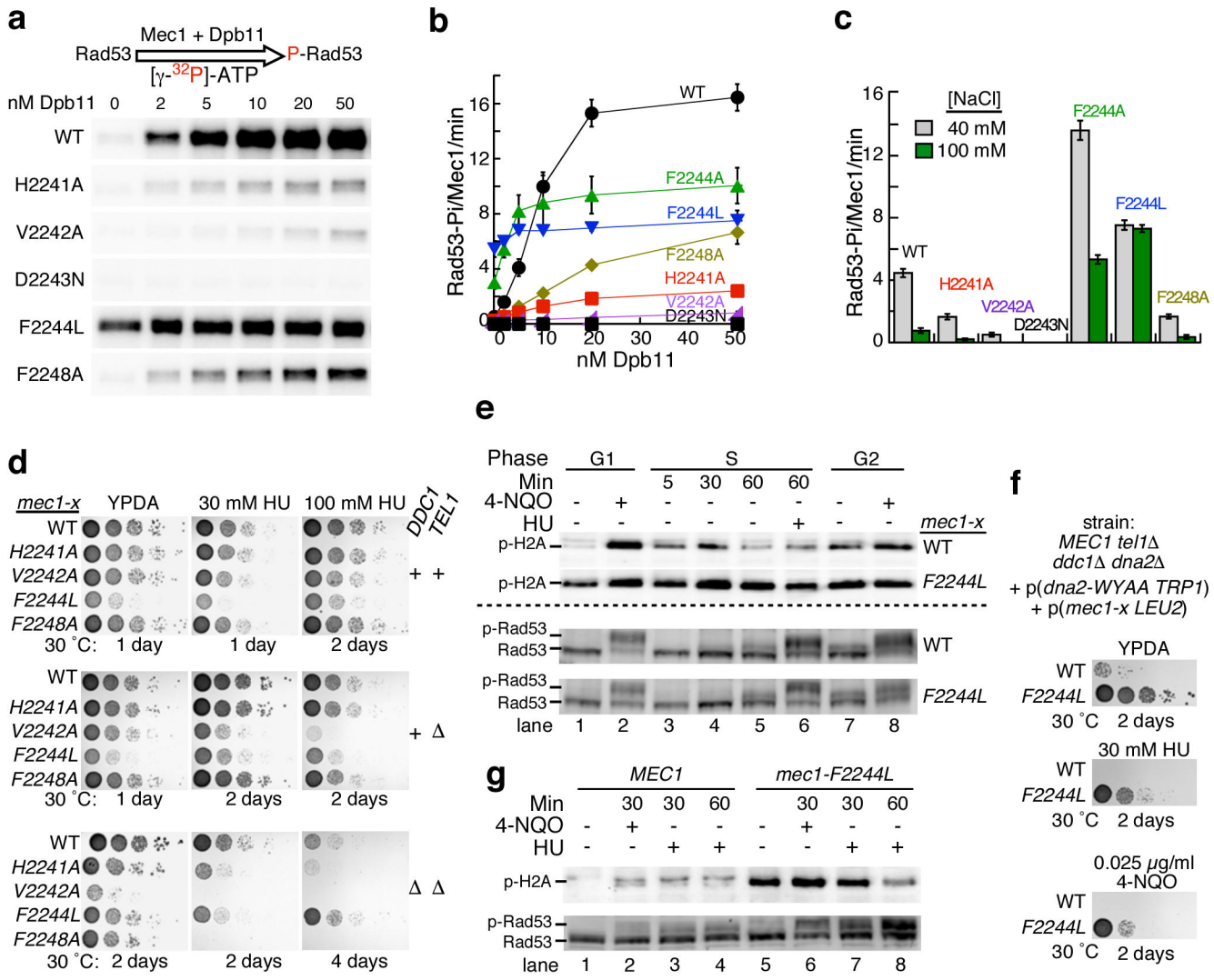

Figure 2: Activation loop mutagenesis of Mec1.

(a) Phosphorylation of Rad53 by Mec1 or Mec1-x mutants with the indicated concentrations of Dpb11 activator. To eliminate contributions by Rad53 kinase itself, the kinase-dead version was used (Rad53-kd, K227A). Example of a full gel is shown in Extended Data Fig. 1a. Uncropped gel images are shown in the Source Data.

(b) Quantification of the data in **(a)** and of analogous assays with the indicated mutants. Activities are expressed as Rad53 phosphates per Mec1 (monomer) per minute.

(c) Phosphorylation of Rad53 in the absence of Dpb11 (Mec1 basal activity), with either 40 mM or 100 mM final NaCl.

(d) Growth of *MEC1* mutants. Strains PY405, PY406, and PY414 are *mec1Δ* and contain plasmid p(*LEU2 mec1-x*). *TEL1* and *DDC1* status is shown on the right. The strains were tested for growth on YPDA plates with or without hydroxyurea as indicated.

(e) Western blot analysis of phospho-H2A (pS129) (top) and Rad53 (bottom) in *tel1Δ* strain PY406, with either wild-type *MEC1* or *mec1-F2244L*. Cells were arrested in G1 phase with alpha-factor, or in G2 phase with Nocodazole, or arrested in G1 phase with alpha-factor, and

released into S phase with or without 200 mM of hydroxyurea. G1-arrested or G2-arrested cells were treated with 4NQO for 30 minutes where indicated (see Methods). Ponceau staining of the blot is shown in Extended Data Fig. 1f.

(f) Growth of activator-defective *MEC1* strain, with relevant genotype shown, on media with or without 4NQO (0.025 μg/ml), or 30 mM hydroxyurea (see also Extended Data Fig. 2b).

(g) Western blot analysis of the same strains. Asynchronously growing cells were treated with 2 μg/ml 4NQO or 200 mM hydroxyurea for the indicated times. Ponceau staining of the blot is shown in Extended Data Fig. 2c.

Error bars for panels b and c represent the standard error of the mean of n=3 independent assays. Uncropped blot images of panels a, e and g and data for graphs in panels b and c are reported as Source Data.

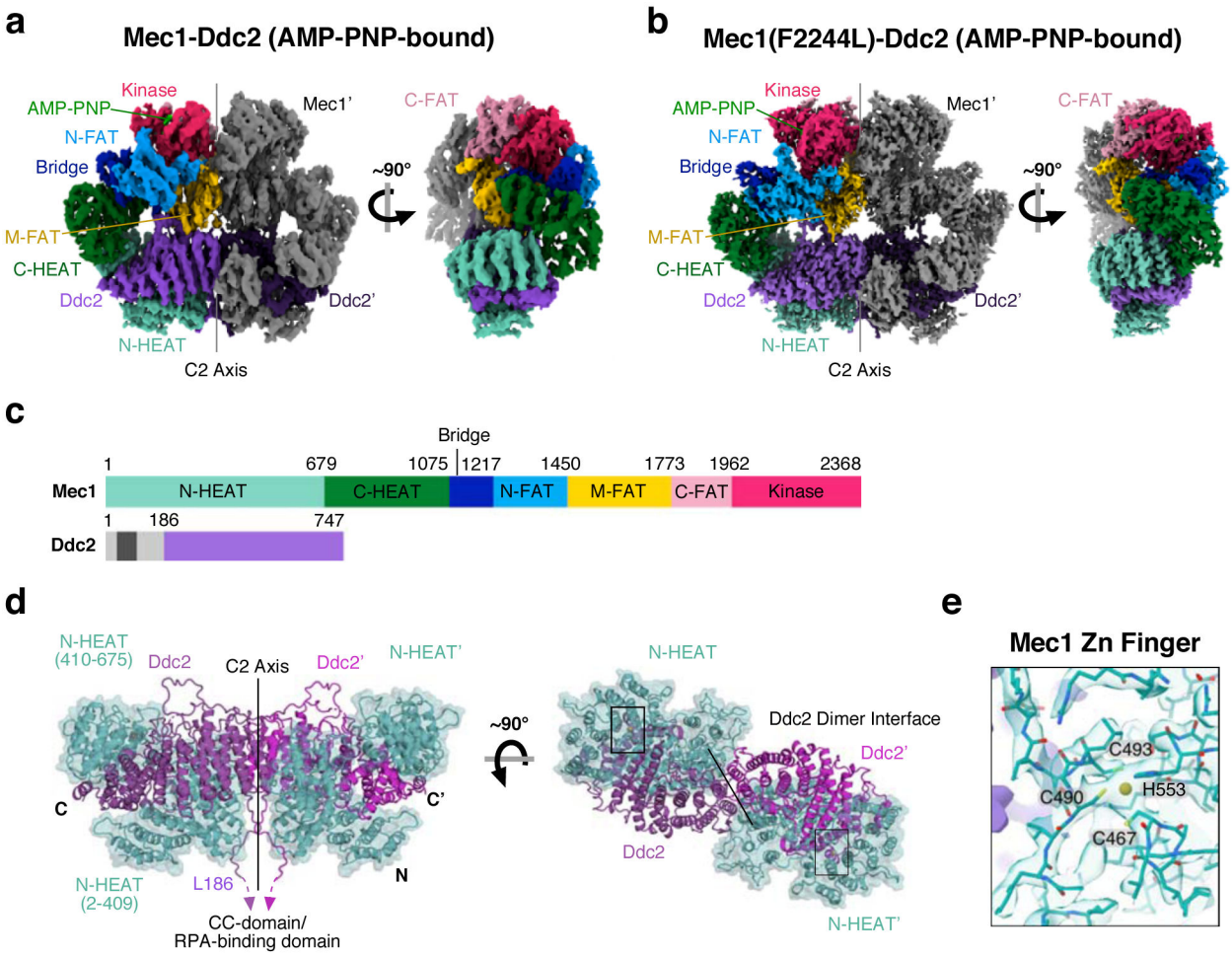

Figure 3: Overall cryoEM structures of Mec1-Ddc2:AMP-PNP and the constitutively active Mec1(F2244L)-Ddc2:AMP-PNP complex.

(a) Two orthogonal views of the Mec1-Ddc2 AMP-PNP-bound complex resolved to 3.8 Å, and **(b)** two orthogonal views of the constitutively active Mec1(F2244L)-Ddc2:AMP-PNP complex resolved to 2.8 Å resolution. Structurally distinct domains are colored; red, kinase; pink, C-terminal-FAT; yellow, Middle-FAT; blue, N-terminal-FAT; navy, bridge; green, C-terminal HEAT; teal, N-terminal HEAT. The Ddc2 subunit is colored purple and the nucleotide colored bright green. The C2 axis is shown. The second Mec1-Ddc2 heterodimer is shown in grey (Mec1') and dark purple (Ddc2').

(c) Primary Structure of Mec1 and Ddc2 proteins showing structural domains and their boundaries.

(d) The Ddc2 dimer is cradled and makes extensive interactions with Mec1 N-HEAT domain. The N-HEAT domain can be divided into two major regions contributing to Ddc2 association (residue ranges are shown). The N-terminal ~170 amino acids, that includes the coiled-coil domain and RPA-interacting motif in Ddc2 is not visible in our structure.

(e) A metal-bound CCHC zinc finger in the Mec1 N-HEAT domain. CryoEM density of the zinc finger region is shown with a coordinated zinc ion.

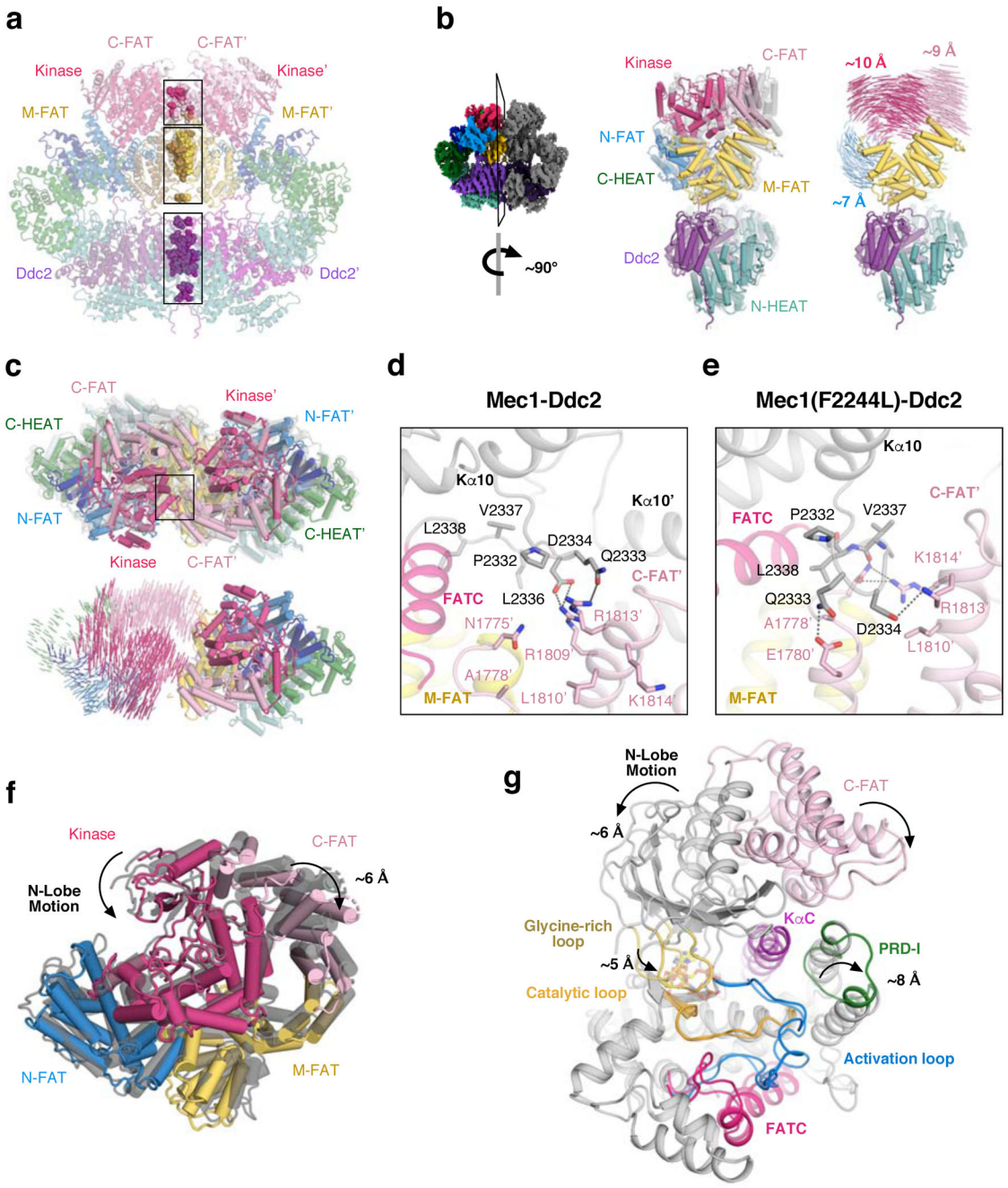

Figure 4: Global domain motions leading to Mec1 constitutive activity.

(a) General dimer interface interactions highlighting three layers; upper layer Kinase:C-FAT ´; middle layer, M-FAT:M-FAT´; Ddc2:Ddc2´ (where ´ denotes the other protomer). Both Mec1-Ddc2 heterodimers are colored by domains as in Fig. 3a.

(b, c) Protomer domain motion between Mec1(F2244L)-Ddc2 and Mec1-Ddc2 (grey), when aligned on a single protomer. Vectors of the motion are shown where the magnitude of the vector corresponds to the rmsd difference for Cα atoms. M-FAT, Ddc2 and N-HEAT show minimal motion (less than 1 Å).

(d, e) Molecular details of the remodeled FATC-PRD loop that forms the kinase:C-FAT' dimer interface between wild-type **(d)** and F2244L **(e)** structures.
(f, g) FAT and kinase domain (FAT-KIN) domain motion and details of the motion in the active site between Mec1(F2244L) and Mec1 (grey) when aligned on the C-lobe. The FAT-KIN is colored by domain as in Fig. 3a and the kinase domain is colored by catalytic feature as in Fig. 1b.

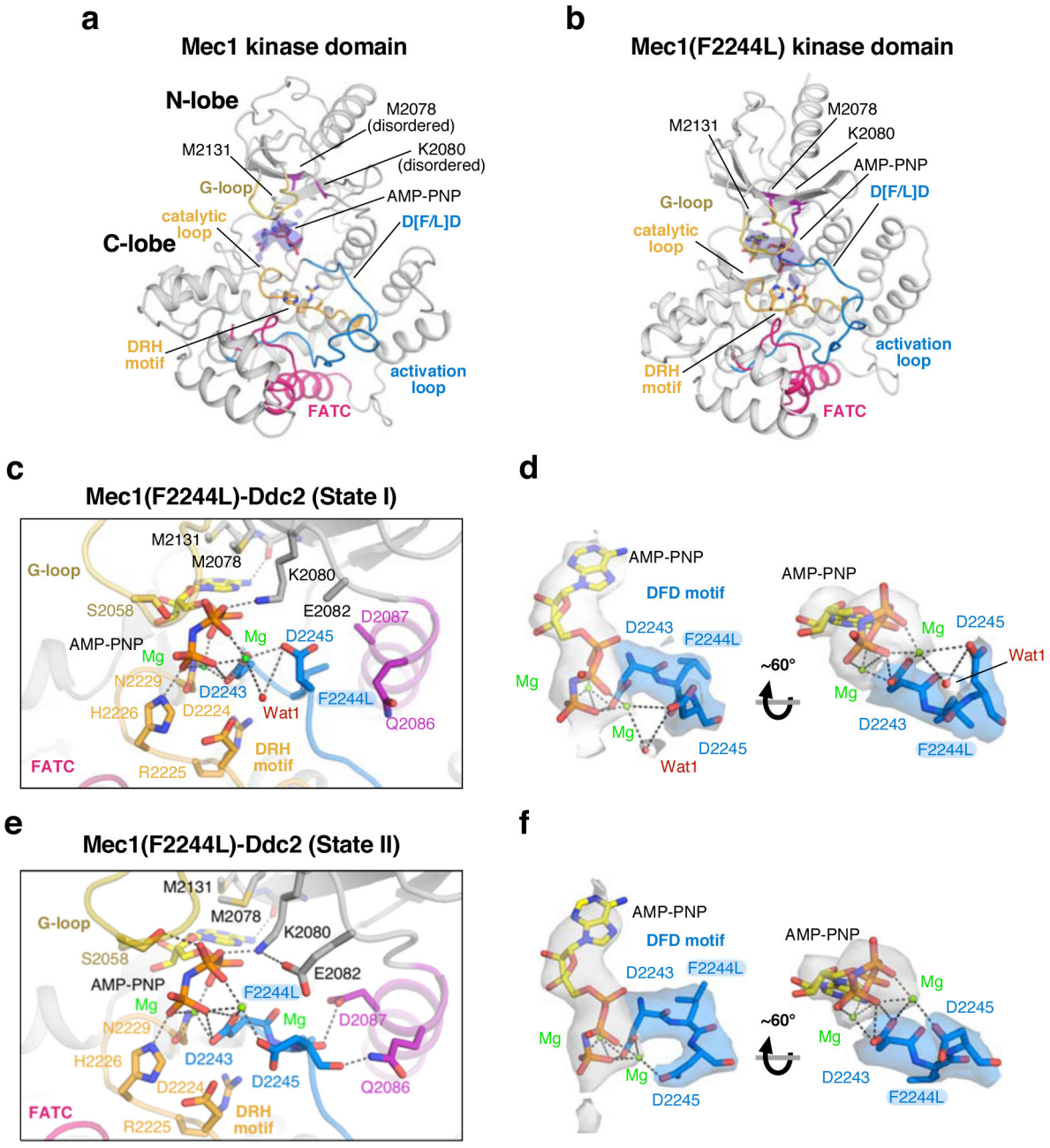

Figure 5: Magnesium-AMP-PNP binding configuration.

(a, b) Relative nucleotide binding sites in the kinase domains of Mec1-Ddc2 **(a)** and the constitutively active Mec1(F2244L)-Ddc2 mutant **(b)**. CryoEM electron density for AMP-PNP (blue) is shown, with locations of catalytically important features (colored and labeled as follows; catalytic loop, orange; activation loop, blue; glycine rich loop, yellow; FATC, magenta) that are contributed by the N-lobe and C-lobe. N-lobe residues, M2078 and K2080, which are not visible in the Mec1-Ddc2 structure are highlighted purple for clarity. The canonical kinase-specific HRD motif is actually DRH in PIKKs (^{2224}DRH^{2226} in Mec1).

(c-f) Molecular details of the Mec1(F2244L)-Ddc2 active site cleft captured in two subtly different states, denoted as State I **(c, d)** and State II **(e, f)**. Nucleotide coordinating residues are shown with H-bonds (dashed lines). The cryoEM density of the mutated DFD motif (F2244L) is shown (blue) to highlight the two conformations of this magnesium coordinating feature. The electron density (shown in grey) corresponding to AMP-PNP and two magnesium ions (green) and coordinated water (red) is also shown. The catalytic features are colored as panels **(a, b**), except that the KαC is colored purple.

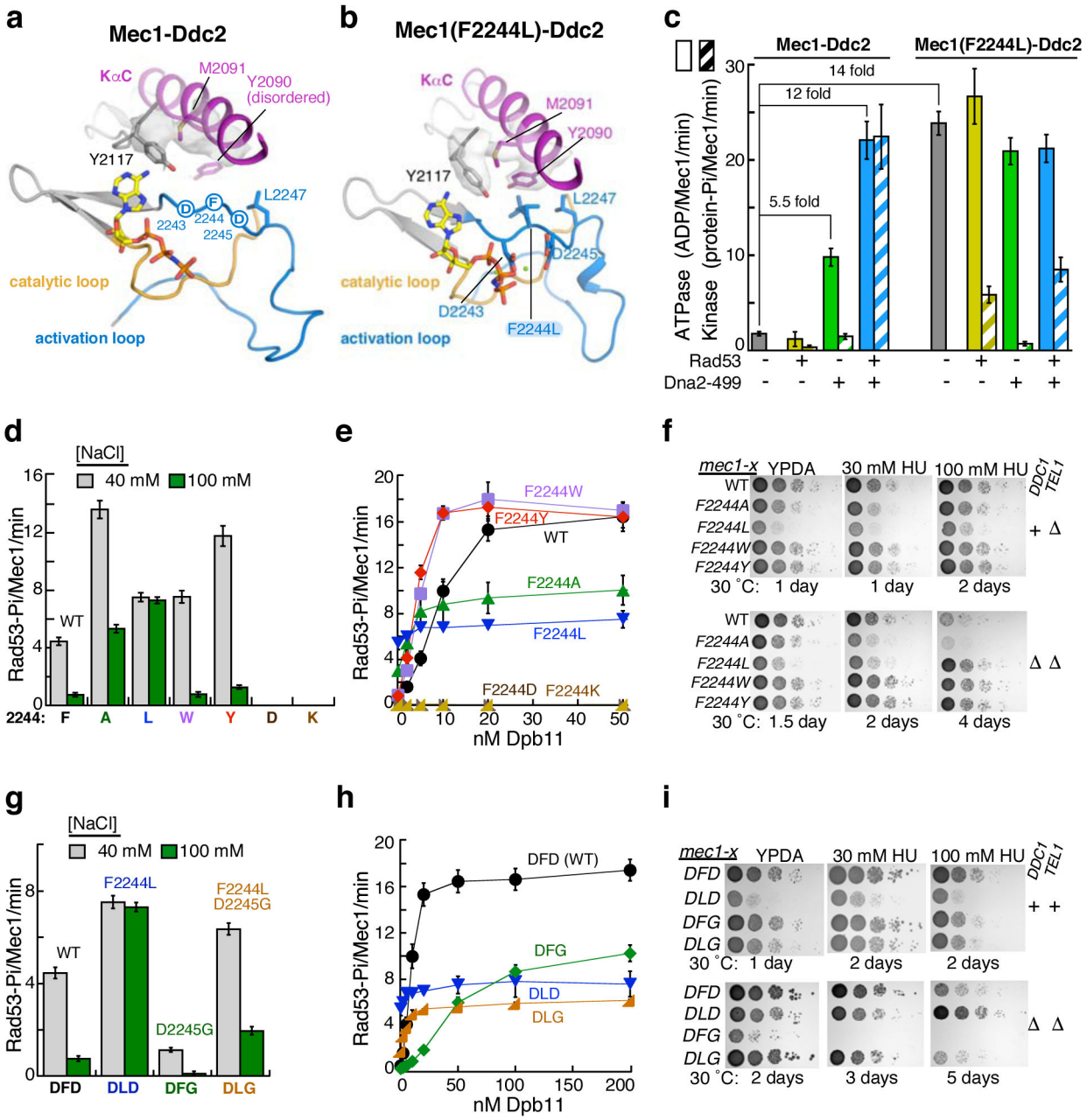

Figure 6: Structure-function analysis of the Mec1 activation DFD loop motif.

(a, b) Conformation of the activation loop (blue) and KαC (purple) showing the residues of the hydrophobic pocket (Y2090, M2091, Y2117 with corresponding cryoEM electron density) that stabilizes residue 2244 of the DFD motif. In Mec1-Ddc2 (A) the exact sidechain position of the DFD motif is not known, and the residues are depicted by spheres. It should also be noted that Y2090 is also not visible, as demonstrated by a lack of density.

(c) Comparative ATPase (solid bars) and kinase (striped bars) activities of Mec1-Ddc2 and Mec1(F2244L)-Ddc2, in the presence or absence of Rad53 and Dna2-499 (see Methods).

(d, g) Basal activity of Mec1 mutants.

(e, h) Dpb11 activation of Mec1 mutants. Half-maximal activation was observed at 10.3 +/− 2.8 nM Dpb11 for wild-type Mec1, 4.3 +/−1.5 nM Dpb11 for Mec1(F2244W), 3.2 +/− 1.1 nM Dpb11 for Mec1(F2244Y) and 95 +/− 25 nM Dpb11 for Mec1(D2245G).
(f, i) Growth of *MEC1* mutants, as described in the legend of Fig. 2.
Error bars for panels c-e, g and h represent the standard error of the mean of n=3 independent assays. Data for graphs in panels c-e, g, and h are reported as Source Data.

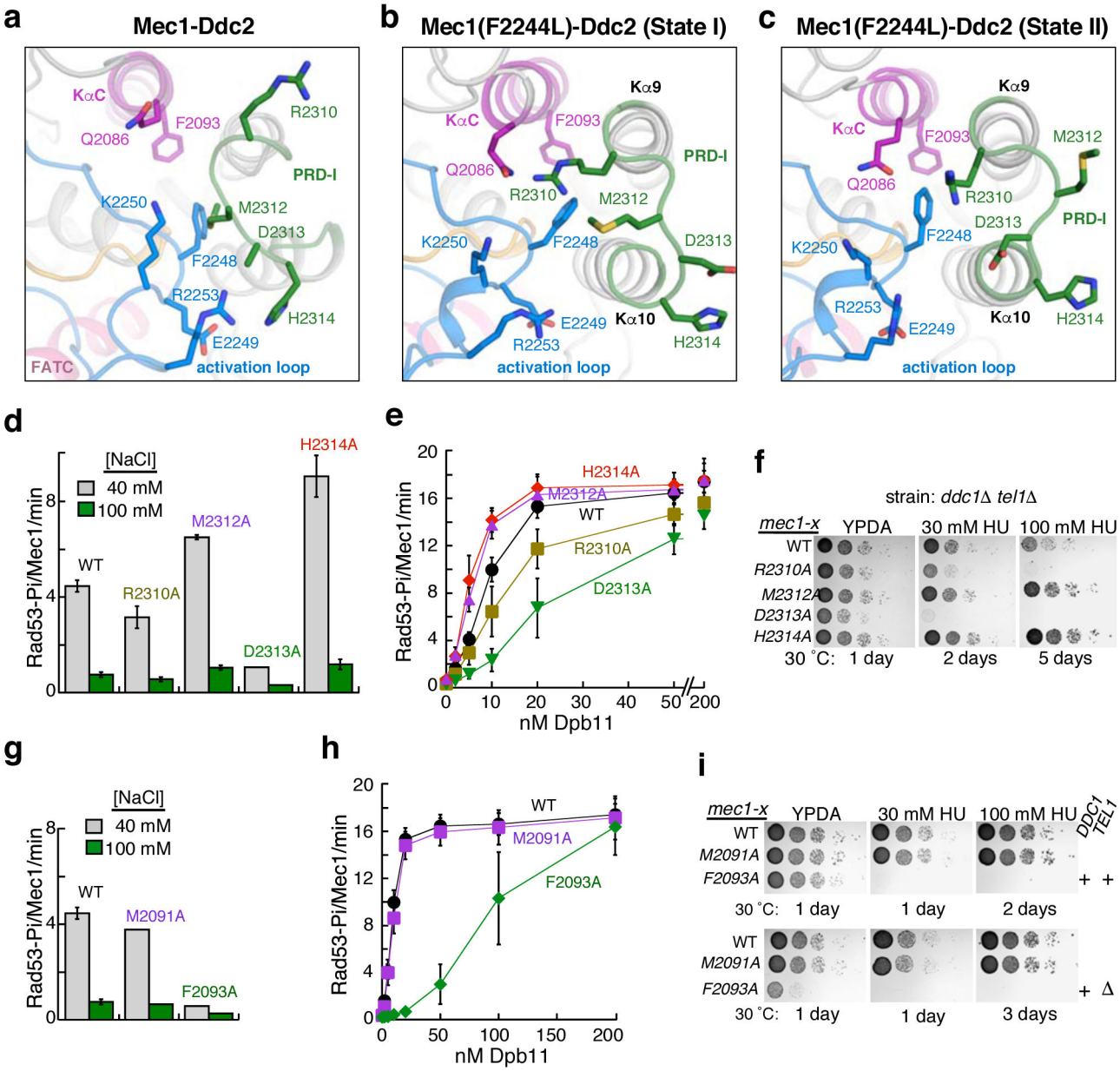

Figure 7: Structure-function analysis of the PRD-I loop and helix KαC (activation loop-interacting helix).

(a, b, c) Molecular details of the PRD-I and the activation loop comparing **(a)** wild-type Mec1 kinase, **(b)** constitutively active F2244L [State I], and **(c)** constitutively active F2244L [State II]. Active site features are colored as in Fig. 5.

(d, g) Basal Mec1 activity. **(e, h)** Dpb11 activation of Mec1. Half-maximal activation was observed at 10.3 +/− 2.8 nM Dpb11 for wild-type Mec1, 15 +/− 3.4 nM Dpb11 for Mec1(R2310A), 5.8 +/− 1.5 nM Dpb11 for Mec1(M2312A), 36 +/− 10 nM Dpb11 for Mec1(D2313A), 5.16 +/− 1.34 nM Dpb11 for Mec1(H2314A), and > 100 nM Dpb11 for Mec1(F2093A).

(f, i) Growth of *MEC1* mutants, as described in the legend of Fig. 2.

Error bars for panels d, e, g and h represent the standard error of the mean of n=3 independent assays. Data for graphs in panels d,e,g, and h are reported as Source Data.

Table 1

CryoEM data collection, refinement and validation statistics

	Mec1(F2244L)-Ddc2 (AMP-PNP bound State I) (EMD-11050 PDB 6Z2W)	Mec1(F2244L)-Ddc2 (AMP-PNP bound State II) (EMD-11051 PDB 6Z2X)	AMP-PNP Mec1-Ddc2 (EMD-11055 PDB 6Z3A)	Mec1-Ddc2 (EMD-11056)
Data collection and processing				
Magnification	81,000	81,000	81,000	75,000
Voltage (kV)	300	300	300	300
Electron exposure (e^{-}/Å^2)	51	51	44	59
Defocus range (μm)	−1.5 to −3.0	−1.5 to −3.0	−0.8 to −2.5	−2.0 to −3.8
Pixel size (Å)	1.06 (0.53 super resolution)	1.06 (0.53 super resolution)	1.06 (0.53 super resolution)	1.09
Tilt angle (°)	0	0	0	0, -30
Symmetry imposed	*C*2	*C*2	*C*2	*C*2
Initial particle images (no.)	~0.9M	~0.9M	~1.9M	~2.0M
Final particle images (no.)	53581	12205	26180	132193
Map resolution (Å)	2.8	3.2	3.8	4.3
FSC threshold	0.143	0.143	0.143	0.143
Map resolution range (Å)	2.5 – 3.7	2.7 – 3.9	3.5 – 5.0	3.5 – 5.0
Refinement				
Initial model used	PDB 5X6O, PDB 4JSP, PDB 6S8F	PDB 6Z2W	PDB 6Z2W	
Model resolution (Å)	3.0	3.5	4.5	
FSC threshold	0.5	0.5	0.5	
Model resolution range (Å)	2.5 – 3.7	2.7 – 3.9	3.5 – 5.0	
Map sharpening *B* factor (Å^2)	−20 to −40	−20 to −60	−40 to −80	
Model composition				
Non-hydrogen atoms	46,588	46,604	46,142	
Protein residues	5,766	5,766	5,730	
Ligands	2 AMP-PNP, 4 Mg^{2+}, 2 Zn^{2+}	2 AMP-PNP, 4 Mg^{2+}, 2 Zn^{2+}	2 AMP-PNP, 2 Zn^{2+}	
B factors (Å^2)				
Protein	57.1	77.4	260.5	
Ligand	99.3	110.2	323.1	
R.m.s. deviations				
Bond lengths (Å)	0.008	0.007	0.007	
Bond angles (°)	1.4	1.1	1.3	
Validation				
MolProbity score	1.83	1.80	2.13	
Clashscore	6.0	5.6	10.6	
Poor rotamers (%)	0.8	0.46	1.04	
Ramachandran plot				
Favored (%)	91.54	91.76	88.84	
Allowed (%)	8.46	8.20	11.7	

	Mec1(F2244L)-Ddc2 (AMP-PNP bound State I) (EMD-11050 PDB 6Z2W)	**Mec1(F2244L)-Ddc2 (AMP-PNP bound State II) (EMD-11051 PDB 6Z2X)**	**AMP-PNP Mec1-Ddc2 (EMD-11055 PDB 6Z3A)**	**Mec1-Ddc2 (EMD-11056)**
Disallowed (%)	0.00	0.03	0.1	